Solid Earth Discuss., https://doi.org/10.5194/se-2019-20
Manuscript under review for journal Solid Earth
Discussion started: 29 January 2019

Distinct Element geomechanical modelling of the formation of sinkhole cluster within large-scale karstic depressions

Djamil Al-Halbouni[1,2], Eoghan P. Holohan[3], Abbas Taheri[4], Robert A. Watson[3], Ulrich Polom[5], Martin P.J. Schöpfer[6], Sacha Emam[7], and Torsten Dahm[1,2]

[1]Helmholtz Centre - German Research Centre for Geosciences (GFZ), Physics of Earthquakes and Volcanoes, Telegrafenberg, Potsdam 14473, Germany.
[2]University of Potsdam, Institute of Geosciences, P.O. Box 601553, Potsdam-Golm 14415, Germany
[3]UCD School of Earth Sciences, University College Dublin, Belfield, Dublin 4, Ireland.
[4]School of Civil, Environmental and Mining Engineering, University of Adelaide, Adelaide, South Australia 5005, Australia.
[5]Leibnitz Institute for Applied Geophysics (LIAG), Stilleweg 2, 30655 Hannover, Germany
[6]Department for Geodynamics and Sedimentology, University of Vienna, Athanstrasse 14, A-1090, Vienna, Austria
[7]Geomechanics and Software Engineer, Itasca Consultants S.A.S, Écully, France

Correspondence to: Djamil Al-Halbouni (halbouni@gfz-potsdam.de)

Abstract

The 2D Distinct Element Method (DEM) code (PFC2D_V5) is here used to simulate the evolution of subsidence-related karst landforms, such as single and clustered sinkholes, and associated larger-scale depressions. Subsurface material in the DEM model is removed by a feedback loop to produce an array of cavities; this simulates a network of subsurface groundwater conduits growing by chemical/mechanical erosion. The growth of the cavity array is coupled mechanically to the surroundings such that cavities can grow also in part by material failure at their margins, which in the limit can produce individual collapse sinkholes. Two end-member growth scenarios of the cavity array and their impact on surface subsidence were examined in the models: (1) cavity growth at the same level and at the same individual growth rate; (2) cavity growth at progressively deepening levels with varying individual growth rates. These growth scenarios are characterised by differing stress patterns across the cavity array and its overburden, which are in turn an important factor for the formation of sinkholes and uvala-like depressions. For growth scenario (1), a stable compression arch is established around the cavity array, hindering sinkhole collapse into individual cavities and favouring block-wise subsidence across the whole cavity array. In contrast, for growth scenario (2), the stress system is more heterogeneous, such that local stress concentrations exist around individual cavities leading to stress interaction. Consequently, sinkhole collapses into individual cavities occurs by shear or tensile failure of the overburden, and these sinkholes lie within a larger scale depression linked to the cavity array as a whole. The results from models with growth scenario (2), which also account for variations in mechanical properties of the overburden, are in close agreement with surface morphological and subsurface geophysical observations from a karst area on the eastern shore of the Dead Sea.

Solid Earth Discuss., https://doi.org/10.5194/se-2019-20
Manuscript under review for journal Solid Earth
Discussion started: 29 January 2019

1 Introduction

Karstification occurs worldwide**,** in soluble rocks like limestone, dolomite, gypsum, anhydrite and salt by chemical dissolution and/or mechanical erosion of subsurface material (BGR et al., 2017). While solution based drainage networks and connected void spaces are hydrologically important for groundwater provision (Chen et al., 2017), such features reduce the mechanical stability of the geologic material and may pose a significant hazard to humans and infrastructure. Underground drainage with subsurface material removal creates typical karst landforms, of whom sinkholes, also termed dolines, are the most prominent (Waltham et al., 2005). They form enclosed small- to large-scale depressions that are morphological expressions of material removal in the underground and subsequent collapse of the overburden (Gutiérrez et al., 2014; De Waele et al., 2011; Waltham, 2016). Often, systems develop into agglomerations of closely spaced dolines and elongated valley-like depressions, potentially revealing linear patterns of drainage (Waltham et al., 2005). Such sinkhole cluster development can be highly dynamic and partly accelerating, and may affect large areas in short times. Understanding their development and where possible precursor signals occur is of utmost importance to mitigate their hazard and for sustainable land and water usage.

The main problem for unravelling the relationships between large-scale depressions and sinkhole development in limestone karst areas, where such landforms have historically been best described, is that the landform evolution is controlled by the relatively slow dissolution kinetics of carbonate minerals. Consequently, the development of these karstic landform types is not directly observable in such areas, and furthermore, it is susceptible to long-term influences from climate change and tectonic activity. Indeed, the areas in which dolines and other karstic depressions have been historically best documented have been modified not only by karst processes but also by fluvial and/or glacial processes.

An opportunity to shed new light on the geometric and genetic relationships between sinkholes, sinkhole clusters and large-scale depressions has arisen with a rapid development at the margins of the shrinking Dead Sea (Yechieli et al., 2016) over the last 40 years. The relatively straightforward tectonic setting and the absence of significant climatic change at the Dead Sea in this time interval drastically reduce any uncertainties associated with such aspects. In several places around the lake there are clusters of tens to over a hundred sinkholes that are surrounded by larger scale (100-800 m diameter) depressions (Al-Halbouni et al., 2017; Atzori et al., 2015; Filin et al., 2011). In particular, recent studies by (Al-Halbouni et al., 2017; Watson et al., 2019) involving field work, remote sensing and photogrammetric surveying enabled the detailed documentation of spatio-temporal relationships between sinkhole and depression development at Ghor Al-Haditha, on the eastern shore of the Dead Sea (Figure 1A). The area exhibits mature karst landforms comprising of individual and compound sinkholes (meaning the nested or non-nested coalescence of sinkholes), lying within gentler, larger-scale (uvala-like) depressions of up to several hundred of meters in diameter, as depicted in Figure 1B and C.

Solid Earth Discuss., https://doi.org/10.5194/se-2019-20
Manuscript under review for journal Solid Earth
Discussion started: 29 January 2019

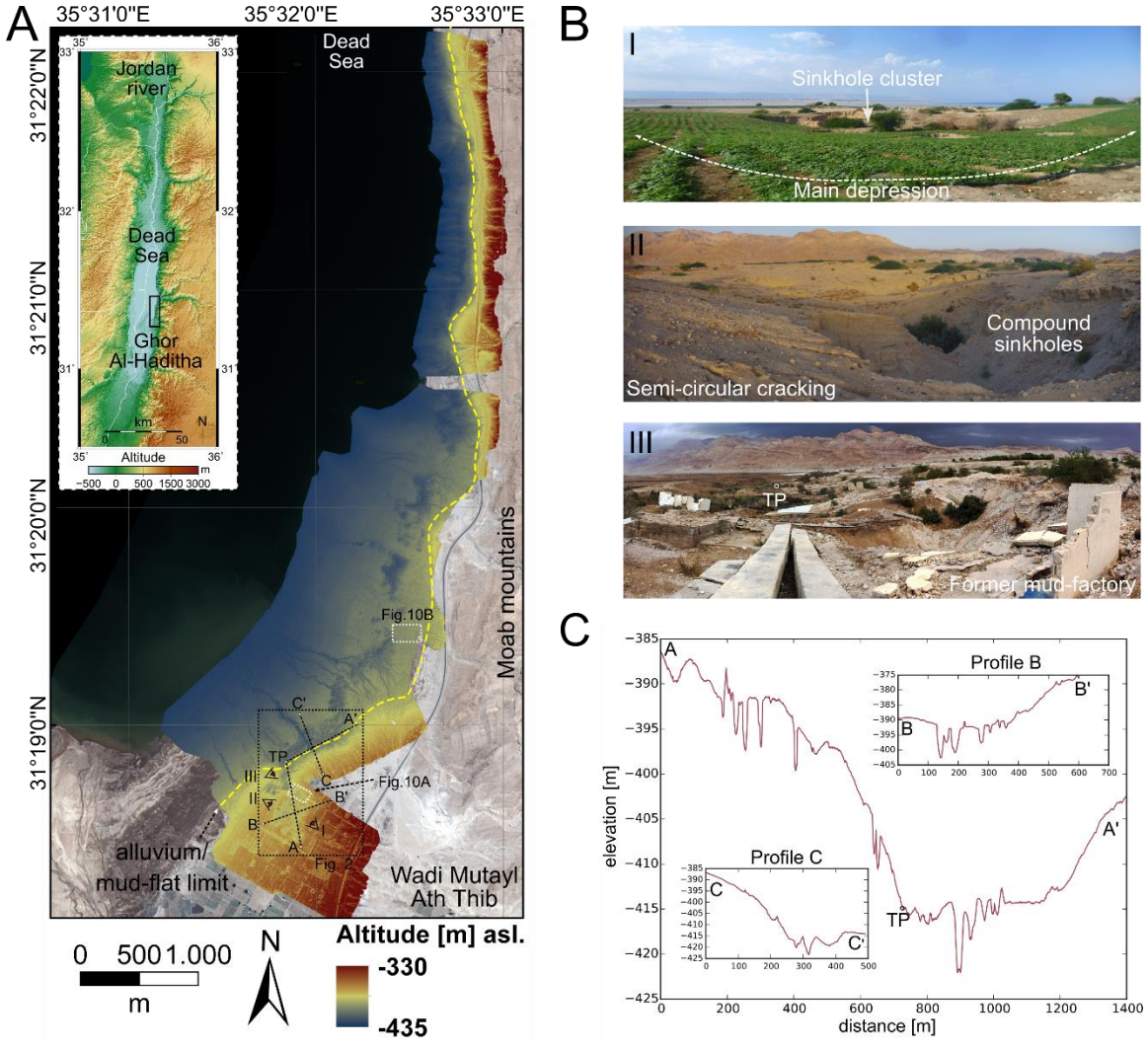

Figure 1: Topography of the Ghor Al-Haditha sinkhole are. (A) Digital surface model (DSM) from 2016 on Pleiades satellite image from 2015 for the sinkhole area at the Dead Sea (inset). The DSM has a resolution of 10 cm px^{-1} and accuracy of 37 and 31 cm (H and V), respectively. The main zone affected by sinkholes extends from S towards the NNE along the contact zone between alluvial fans and the mudflat (dashed yellow line) and comprises of several partly connected large depression zones, of which the main area is indicated by the square. (B) Typical examples of sinkhole formations in the main depression. (I) View from the stable agricultural area towards the centre of the depression. (II) Nested sinkholes and ground cracks from the opposite view. (III) Destroyed "Numeira" mud factory at the turning point (TP) of the depression. (C) N-S and E-W topographic profiles across the several hundred meter depression, derived from the DSM of 2016.

Initially, these features develop as small localised subsidence, with single sinkholes that form in heterogeneous material compositions made of Dead Sea mud, alluvial fan sediments and salt (Watson et al., 2019). Larger-scale subsidence and sinkhole clustering follows, with ground fracture systems developing that are geometrically related to the larger scale depression rather than to individual sinkholes or sinkhole clusters (Figure 2). The evolved system typically shows dense

Solid Earth Discuss., https://doi.org/10.5194/se-2019-20
Manuscript under review for journal Solid Earth
Discussion started: 29 January 2019

distributions of multiple sinkholes of different sizes (1-70 m in diameter). The cover material may show marginal curved to linear fracture traces related to the ground subsidence on both scales.

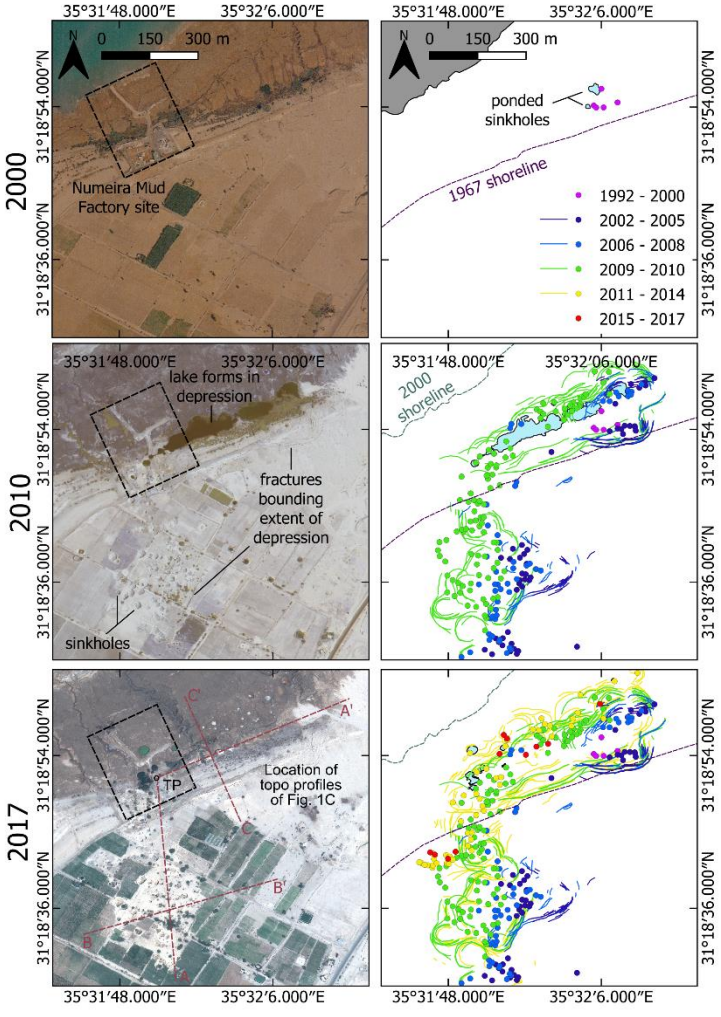

Figure 2: Remote sensing analysis of the evolution of sinkholes, cracks and large depressions at the main depression of Ghor Al-Haditha, Dead Sea. Small single sinkholes appear in 2000 at the former "Numeira" mud factory site (0.6 m/pix aerial photo from Royal Jordanian Geographic Centre). Up to 2010, lakes, sinkhole clusters and large fractures have appeared around a depression zone spanning over both alluvium and mud-flat (0.5 m/pix GeoEye-1 satellite image). Up to today, the number of fractures and sinkholes as well as the depth of the depression has increased (0.5 m/pix Pleiades satellite image).

In this paper, we test the hypothesis that the driving process for the geomorphological and structural development of such large-scale karst features is a widespread, differential subsidence above an array of sub-surface cavities, with temporally- and spatially variable patterns of material removal driven by base-level fall associated with the shrinking of the Dead Sea.

To test our hypothesis, we undertook novel numerical modelling using the 2D distinct element method (DEM). We examine two end-member growth scenarios of model cavity arrays, and we look at the surface morphologies, sub-surface structure and

stress patterns developed by subsidence of the overburden as those cavity arrays grow. The numerical results are discussed with examples from the Dead Sea salt karst. Recent shear wave reflection studies revealed in the area of Ghor Al-Haditha a highly scattered subsurface with bowl, fracture and depression structures in the deep-shallow underground of a typical prograding Gilbert type delta (Polom et al., 2018). We provide in this work both a qualitative and quantitative comparison of the results from the seismic survey and from the numerical modelling. We show that our scenario (2) is able to explain complementary observations from surface morphology to subsurface hydrology and subsurface geophysics.

2 Numerical approach

2.1 Distinct Element Method Numerical Modeling

The mechanical interaction of a single void space with its surrounding rock mass hereby has been thoroughly investigated by analytical methods (Tharp, 1999) and numerical modelling studies (Al-Halbouni et al., 2018; Baryakh et al., 2009; Fazio et al., 2017; Hatzor et al., 2010; Parise and Lollino, 2011). Little is known, however, about the mechanical relationships between multiple actively evolving void spaces in the sub-surface and how these may lead to the development of sinkhole clusters and large-scale depressions. Moreover, commonly-used continuum numerical simulation methods are usually not appropriate to simulate rotation, detachment and non-continuous deformation found in rocks or semi-consolidated materials subject to large strains. Discontinuous medium simulation methods, on the other hand, allow for complex behaviours like spontaneous crack formation and block rotation (Jing and Stephansson, 2007). Distinct Elements (Cundall, 1971) is a subset of Discrete Element Modeling (Cundall and Strack, 1979; Jing and Stephansson, 2007) whereby a material is represented by an assembly of non-deformable particles in the shape of disks of unit thickness (2D, Figure 3) or spheres (3D). The particles are assigned a density, radius and an elastic contact modulus. They are distributed with a certain porosity and follow a defined size distribution. In our case, we use a uniform distribution between a minimum and maximum particle radius in a 2D box. The particles follow the Newton-Euler laws of motion and the linear force-displacement law as they interact elastically at each contact point. The assembly is generated via a gravitation settling scheme (Al-Halbouni et al., 2018), after which particles can be bonded with their neighbours (Potyondy and Cundall, 2004). In this study, we used the parallel-bond model (PBM) in the commercially available software PFC2D (Potyondy, 2014), which sets a second pair of elastic springs that incorporate moments and can fail either in shear or tension, allowing for complex deformation patterns to build. The resulting differential equations are solved via a finite difference explicit time-stepping algorithm (Jing and Stephansson, 2007). Each model requires multiple realisations as the outcomes generally depend on the randomised particle packing. For more mathematical details on the calculations and modelling scheme refer to (Al-Halbouni et al., 2018; Itasca Cooperation Group, 2014; Jing and Stephansson, 2007; Potyondy, 2014; Wang et al., 2018).

Solid Earth Discuss., https://doi.org/10.5194/se-2019-20
Manuscript under review for journal Solid Earth
Discussion started: 29 January 2019

2.2 Cavity growth in a DEM model

Al-Halbouni et al., 2018, implemented the growth of a single cavity in a DEM model and conducted a detailed calibration and verification procedure to determine the optimal model geometry, resolution and material removal technique. We here adopt the same setup parameters and conditions: i.e. model height H x width W = 400 x 400 m; a mean particle radius of $\bar{R} = 0.32$ m; initial porosity of the unsettled assembly of n = 0.2; no-slip boundary conditions; and a fixed wall elastic modulus of $E_w =$ 5 GPa. Instead of simulating material removal in a single void as in *Al-Halbouni et al.*, 2018, however, we here implemented the quasi-static, incremental growth of an array of multiple cavities of arbitrary shape (Figure 3, cf. Appendix A.1). Our 2D model thus represents a flow-perpendicular cross-section through a branched conduit flow network, which has resulted from dissolution that rapidly localised through a feed-back mechanism of enhanced fluid flow with increasing dissolution (Weisbrod et al., 2012) and which in turn can also promote conduit growth by physical erosion.

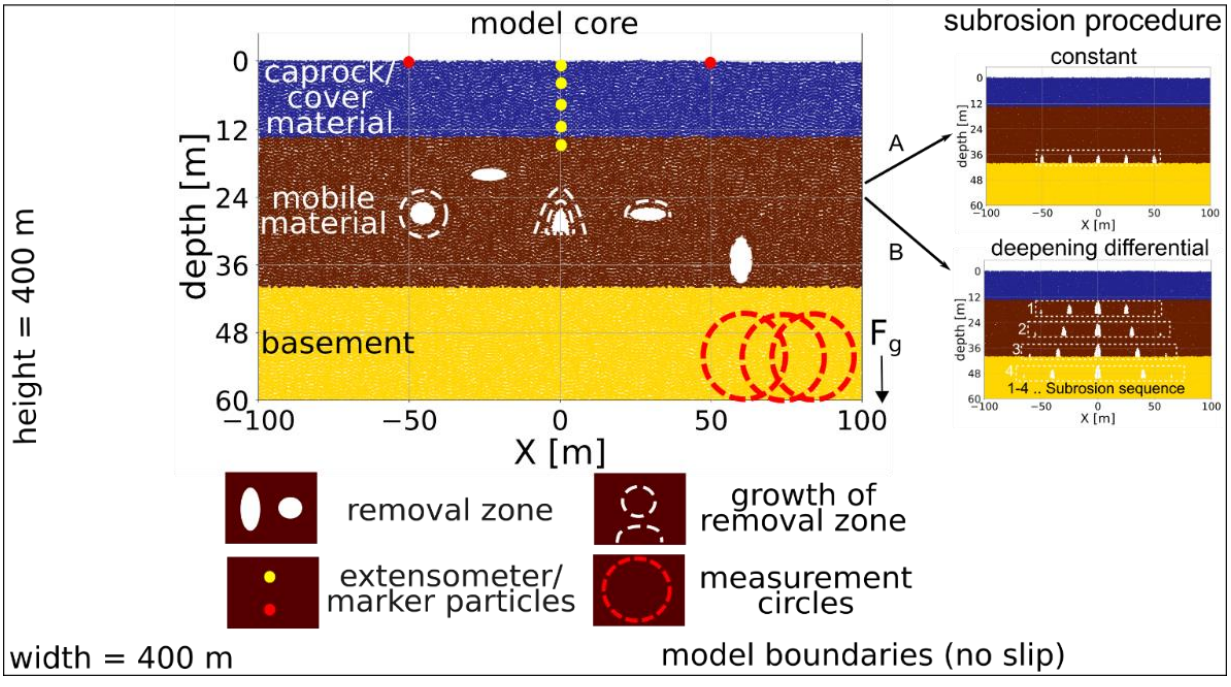

Figure 3: Generic setup for multiple void space modelling with DEM. The core of the model and the specific setup of the void zone and implemented features are shown here. Arbitrary material removal zones can be defined and associated with different removal functions activated at arbitrary dissolution zone growth increments. The subrosion procedures for (A) "Standard" model with deep constant subrosion and (B) "Complex" subrosion with deepening sequence and differential void space growth are highlighted.

We test two end-member growth scenarios of the cavity array and their impact on surface subsidence in the models: (1) cavity growth at the same level and at the same individual growth rate (Figure 3A); (2) cavity growth at progressively deepening levels with varying individual growth rates (Figure 3B). In the first scenario, five semi-elliptical cavities begin to grow at the same time, at the same constant rate, and at the same depth of 40 m. In the second scenario, the five start to grow simultaneously, but the initial cavity area is largest in the centre and decreases laterally. In addition, the cavity growth rate is

Solid Earth Discuss., https://doi.org/10.5194/se-2019-20
Manuscript under review for journal Solid Earth
Discussion started: 29 January 2019

largest for the central cavity and smallest for the outermost cavities. This represents the energy distribution of a progressively focussed flow within the growing conduit system. Furthermore, new cavity arrays develop at progressively increasing depths from 20 m to 50 m at 10 m increments. The growth in the shallower cavity array stops when the new array initiates. The 30 m deep array initiates after a total volume removal of ~ 400 m³, the 40 m deep subrosion starts after ~ 800 m³ and the 50 m deep subrosion scheme starts after ~ 1200 m³. The width of the array also increases slightly from ~110 m in the shallow part to ~150 m in the deep part. This progressive initiation of newer and deeper arrays represents a vertical evolution of subrosion front during a base-level fall, the main hydrogeological boundary condition at the shrinking Dead Sea (Watson et al., 2019).

2.3 Material parameters

The bonded particle assembly's bulk material properties, which emerge from the properties defined on the particle scale, were constrained by simulated rock tests on material samples (Schöpfer et al., 2007; Al-Halbouni et al., 2018). Parallel-bond tensile strength, modulus and friction, cohesion and friction angle, as well as contact modulus and friction, are hence transferred to corresponding bulk values of unconfined compressive strength (UCS) and tensile strength (T), Poisson's ratio (ν) and Young's modulus (E). This calibration procedure has been done for three materials representing those most common at the Dead Sea shoreline (see Al-Halbouni et al., 2018 for details): (1) low-strength clayey mud of the former Dead Sea lakebed, (2) middle-strength sandy-gravel alluvial fan sediments and (3) relatively higher strength Holocene rock salt of the Dead Sea (Table 1). For (1) a bond healing procedure has been implemented to account for a more realistic recombination behaviour of naturally wet muddy material.

Table 1: Estimated mean bulk geomechanical properties of the main materials in sinkhole-affected areas at the Dead Sea. The variation of the bulk strength values is related to analysis by both Mohr-Coulomb and Hoek-Brown failure criteria assuming intact rock and together with the error estimates can be found in Al-Halbouni et al., 2018.

Parameter	Symbol	Unit	Wet lacustrine mud	Alluvial sediment	Holocene Salt
Particle packing porosity	n_{eff}	-	0.21	0.2	0.17
Bulk density	ρ_{bulk}	[kg/m^3]	2145	2200	2075
Young's modulus	E_{eff}	[GPa]	0.084 ± 0.02	0.174 ± 0.025	1.106 ± 0.126
Poisson's ratio	ν_{eff}		0.19 ± 0.12	0.31 ± 0.6	0.30 ± 0.03
Unconfined compressive strength	UCS	[MPa]	-0.25 to -0.06	-0.92 to -0.52	-1.54 to -1.23
Unconfined tensile strength	T	[MPa]	0.01-0.2	0.18-0.24	0.31-0.43
Cohesion	c	[MPa]	0.11	0.18	0.36
Friction angle	ϕ	[°]	5.7	22.3	28.8

Solid Earth Discuss., https://doi.org/10.5194/se-2019-20
Manuscript under review for journal Solid Earth
Discussion started: 29 January 2019

2.4 Geophysical parameter tracking

Distributed measurement circles of area A_{MC} are used to record stresses, strain rates and porosity in the DEM simulations (see Al-Halbouni et al., 2018 for details). Here we use porosity tracking results to determine apparent elastic moduli, which can then be translated via bulk density into apparent bulk seismic velocities. In general, for a homogeneous, linearly-elastic, isotropic medium, seismic wave velocities are estimated by:

$$v_s = \sqrt{\frac{G}{\rho}}$$

$$v_p = \sqrt{\frac{K+\frac{4}{3}\nu}{\rho}} = \sqrt{\frac{2G(1-\nu)}{\rho\,(1-2\nu)}}$$

K, G are the bulk/shear modulus, respectively. $E = 2G(1+\nu)$ is Young's elastic modulus for homogeneous, isotropic materials, with ν as the Poisson ratio. ρ is the bulk density calculated by $\rho = \rho_{particle}\,(1-n)$, with n as the particle packing porosity. A correction factor is needed to account for the differences between static and dynamic moduli to enable a comparison of numerical simulation with field data. Dynamic field methods like seismics measure at small strains and therefore reveal high values of the shear modulus. E and ν of the model materials are known from simulated large-strain compression tests for a variation of confining pressures and porosities (Al-Halbouni et al., 2018). We here use $G_{dyn} \sim 1.5 * G_{stat}$, the dynamic shear modulus, approximated as a minimum scaling of the static shear modulus determined for unconsolidated sand in a cycling loading/unloading and shearing test (Soldal and Mondol, 2015). The factor depends on the applied static technique in laboratory experiments and on the cycles, the difference rises mainly from the strain amplitude (Hammam and Eliwa, 2013; Wichtmann and Triantafyllidis, 2009). Furthermore, from the simulated compression tests, usually conservative values for moduli and Poisson ratio are taken at limits where no or little amount of cracks have appeared in the sample. For a more realistic approach, the values are further adjusted by accounting for the crack (broken bond) density in the model, following *Dahm and Becker*, (1998). For the adjustment to the DEM, crack density is defined as $c = {k\pi\bar{R}}/{A_{MC}}$, with k as the number of cracks, A_{MC} the area of the measurement circle and $\bar{R}$ as the mean particle radius, which is a proxy to the parallel-bond (crack) half length (see *Al-Halbouni et al.*, (2018) for details). Cracks, i.e. broken parallel bonds in DEM, are recorded by using an intrinsic "fishcall" procedure (Hazzard, 2014; Hazzard and Young, 2004), and distributed onto the according measurement circles. With increasing crack density, ν is expected to increase and the apparent (effective) shear modulus G_{eff} is expected to decrease by:

$$\nu(c) = \frac{(1-\nu_0)e^{\frac{fc}{2}} + 2\nu_0 - 1}{2(1-\nu_0)e^{\frac{fc}{2}} + 2\nu_0 - 1}$$

$$G(c)_{eff} = G_0/(2(1-\nu_0)e^{\frac{fc}{2}} + 2\nu_0 - 1)$$

With f = 0.5, $\nu_0 = 0.5$, the Poisson ratio and G_0, the shear modulus of the homogeneous, isotropic rock mass.

Solid Earth Discuss., https://doi.org/10.5194/se-2019-20
Manuscript under review for journal Solid Earth
Discussion started: 29 January 2019

3 Modeling Results

In this section we present outcomes of both end-member cavity growth scenarios, while focussing on a final best model setup to achieve the above-mentioned typical karst landforms (Sec. 0). For both end-member cavity growth scenarios, we show the results of models for layered combinations of weak and strong materials common at the Dead Sea shoreline.

3.1 Structural and morphometric features in end-member scenarios of cavity array growth

In Figure 4 we compare the outcomes of both end-member cavity growth scenarios for four different material setups representing weak and strong overburden configurations: alluvium on lacustrine mud (Figure 4A), a thin salt-layer above lacustrine mud and alluvium (Figure 4B), pure lacustrine mud (Figure 4C) and a mud layer above a salt and alluvium succession (Figure 4D). In this overview, a clear difference between scenario (1), constant medium-depth (40 m) subrosion, and scenario (2), a differential deepening subrosion, can be seen. While scenario (1) results in block-wise subsidence or large-scale sagging, scenario (2) reproduces the observed pattern of multiple sinkholes in a large-scale depression zone. The main structural features that relate to differences both in material and in subrosion scenario are marked in each individual plot.

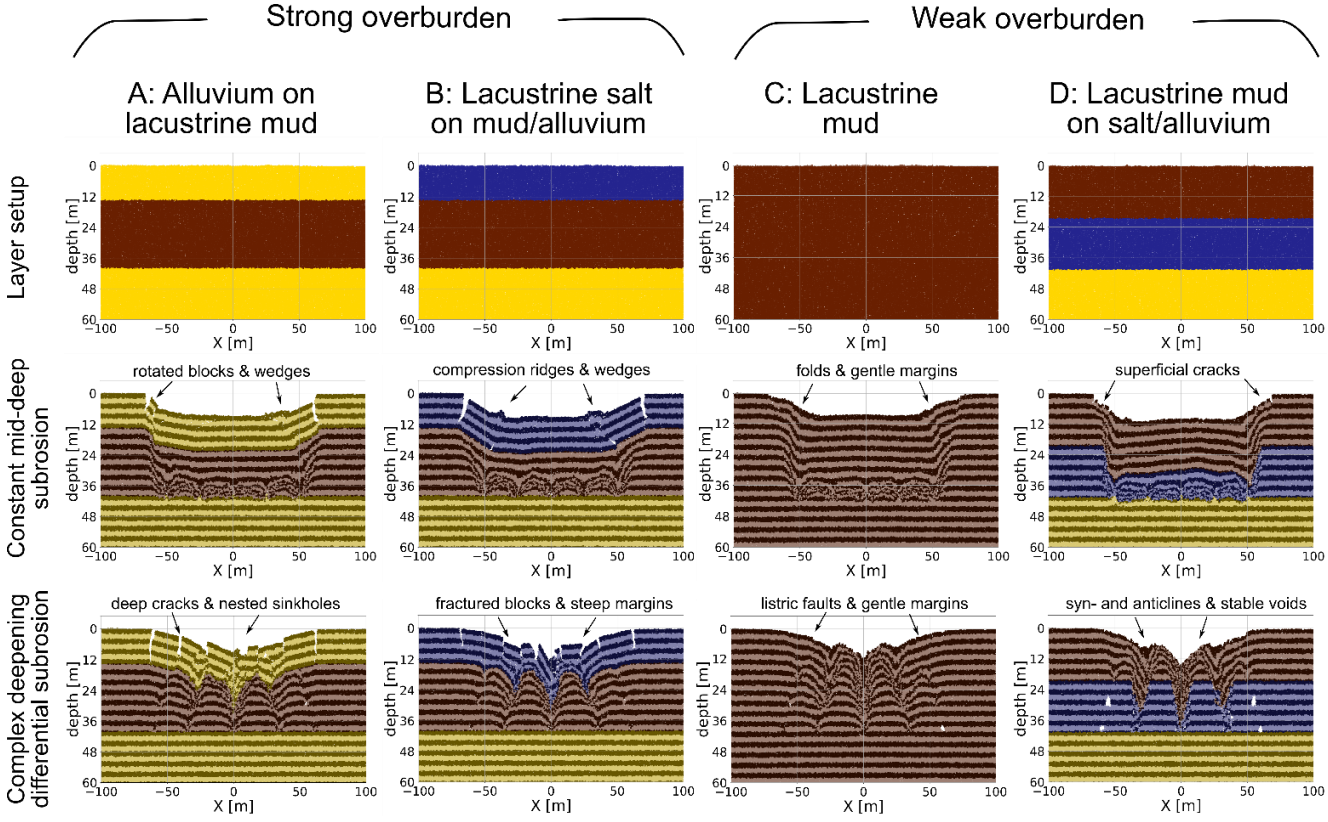

Figure 4: Comparison between final results for two subrosion setup endmembers and different material compositions common at the Dead Sea shoreline. The removed volume at the shown stages is approximately 900 m^3. Strong overburden: (A) alluvium/mud succession and (B) salt on mud/alluvium succession. Weak overburden: (C) pure lacustrine mud and (D) mud on salt/alluvium succession. Note that passive marker layers are applied to highlight structural features.

Solid Earth Discuss., https://doi.org/10.5194/se-2019-20
Manuscript under review for journal Solid Earth
Discussion started: 29 January 2019

In Figure 5 we show the evolutionary stages I-VI of sinkhole/depression development for cavity growth scenario (2), i.e. the deepening differential subrosion scenario. For all combinations of material, the large-scale depression is deepest throughout the evolution above the central and fastest growing cavity in each array (as per definition in the model setup).

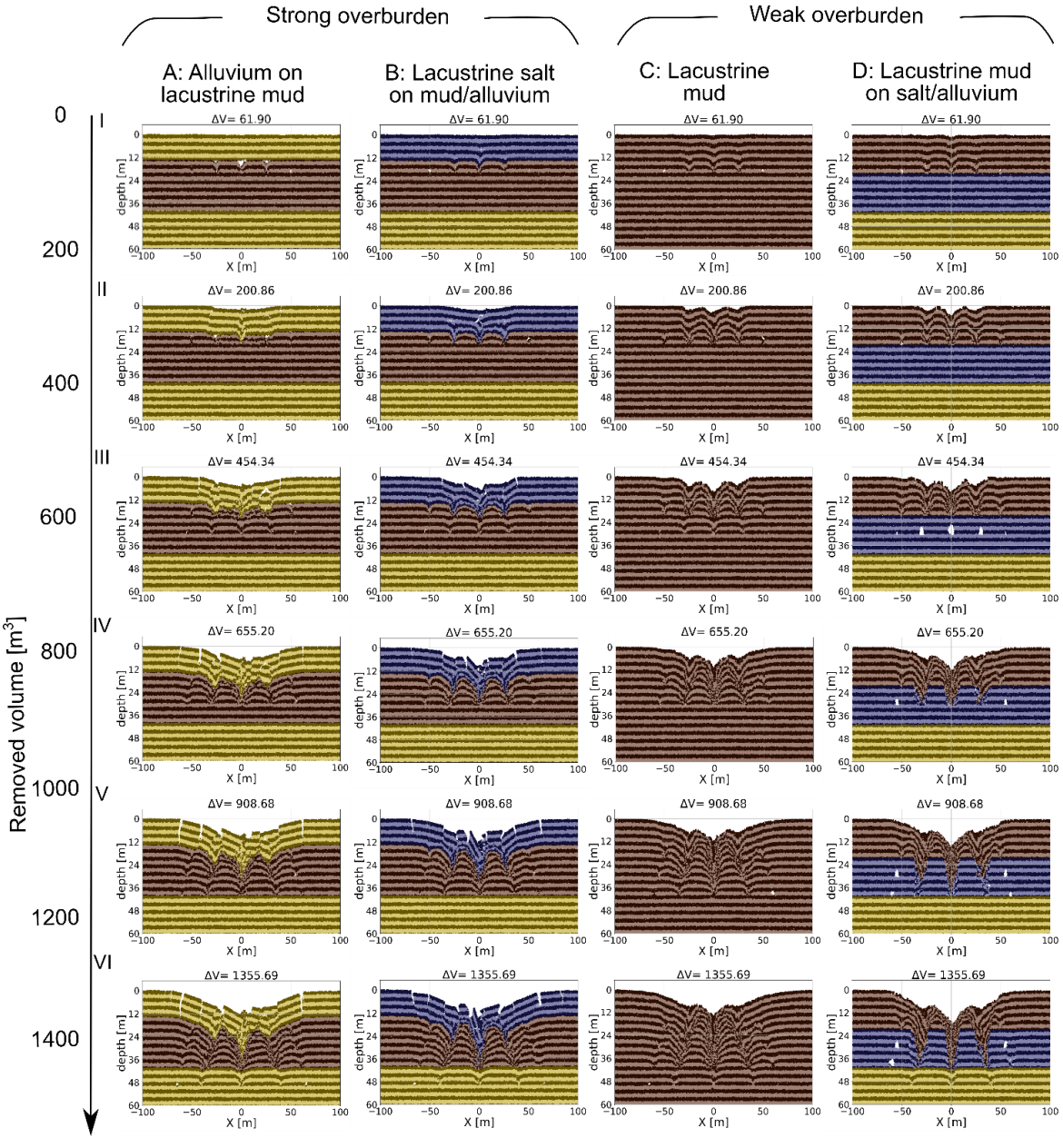

Figure 5: Final model sinkhole evolution results for four different material combinations common at the Dead Sea shoreline. Strong overburden: (A) alluvium/mud succession and (B) salt on mud/alluvium succession. Weak overburden: (C) pure lacustrine mud and (D) mud on salt/alluvium succession. The removed volume [m^3] is shown above the plots. Note that passive marker layers are applied to highlight structural features.

In general, for the material combination of strong or weak overburden above weak cavity host material (Figure 5A-C), individual sinkholes form synchronously with, or just before, the development of a larger-scale synclinal depression that initially spans several cavities and eventually spans the cavity array as a whole. The formation of the sinkholes more clearly predate the array-scale depression where the overburden is weak. The margins of the array-scale synclinal depression are commonly delimited, especially in the strong overburden, by fractures and/or faults. These marginal fractures geometrically relate to subsidence across several cavities, or to subsidence across the entire array, rather than to collapses into individual cavities. In weaker overburden, the margins of the main depression are defined by inward bending (sagging) of the overburden layers (although in detail there are many small-scale fractures here).

For the material combination of weak overburden above a strong cavity-hosting material (Figure 5D), however, large cavities can develop before the overburden collapses into them. This produces deeper and sinkholes in the later stages of the model evolution. Also in this case, the strong cavity-hosting material does not deform so easily around the cavity array as a whole, and therefore synclinal bending of the overburden across the cavity array is much less pronounced. Consequently, the larger-scale depression forms in this case mainly by nesting and coalescence of the sinkholes.

For individual sinkholes in strong overburden materials (Figure 5A, B), the collapsed overburden is commonly delimited by faults near the surface, but at depth the collapsed overburden structure takes a synclinal form (V-shaped) on the same scale of the individual cavities. For individual sinkholes in weak overburden material (Figure 5C, D), the collapsed overburden shapes are synclinal at all depths. These cavity-scale synclinal structures represent the downward flow of the weak material into the cavities or, where cavity formation is inhibited, into the zones of material removal. In the strong cavity-hosting material (Figure 5D), the deep-levels of the individual collapse zones are again in part fault-bounded but also take in part a synclinal form.

Depth to diameter (De/Di) ratios of both simulated sinkholes and depressions are given in Table 2 as mean values of 3-5 model assemblies of each material combination. Only depressions at the scale of the cavity-array are considered, their sizes range from ~ 65-190 m across and ~ 2 – 18 m deep, while sinkholes occur on scales of ~ 1.5-36 m across and ~ 0.5-12 m deep. Higher De/Di ratios of 0.48 – 0.64 for sinkholes are generally recorded for cover material of higher strength (alluvium, salt), while lower ratios of 0.22-0.24 are found for low strength cover material (mud). De/Di ratios of the depressions are generally an order of magnitude lower than those of the sinkholes and closer to each other. However, a trend from low De/Di ratios at early stages of the simulation to higher De/Di ratios at late stages is observed, with a considerable divergence dependent on the subsurface material.

Solid Earth Discuss., https://doi.org/10.5194/se-2019-20
Manuscript under review for journal Solid Earth
Discussion started: 29 January 2019

Table 2: Depth to diameter ratios of simulated sinkholes and array-scale depressions. The average results for the four different material setups and different stages of depression development are given. The depth of a depression is hereby considered the deepest point, which might coincide with the deepest point of a sinkhole. The diameter goes as far as any vertical surface displacement can be observed.

Type/Model setup	Lacustrine mud	Alluvium on mud	Salt on mud/alluvium	Mud on salt/alluvium
Early stage depression	0.06 ± 0.007	0.03 ± 0.01	0.04 ± 0.01	0.07 ± 0.01
Middle stage depression	0.07 ± 0.003	0.07 ± 0.01	0.09 ± 0.01	0.11 ± 0.01
Late stage depression	0.07 ± 0.01	0.09 ± 0.01	0.11 ± 0.01	0.14 ± 0.01
Final stage sinkholes	0.22 ± 0.12	0.48 ± 0.36	0.64 ± 0.3	0.24 ± 0.08

The evolution trend for large-scale depressions (Figure 6) shows the influence of the material strength on geometrical aspects of the large-scale depressions. A clear divergence can be observed between mud subsurface and salt subsurface models. A mechanically weak subsurface (mud) affects the geometry of void space formation in the subsurface and a more conical void space forms, giving space for lateral widening of the depression. A mechanically strong (salt) subsurface inhibits the synclinal bending at the margins of the main depression and would lead to deepening of the depressions preventing the widening.

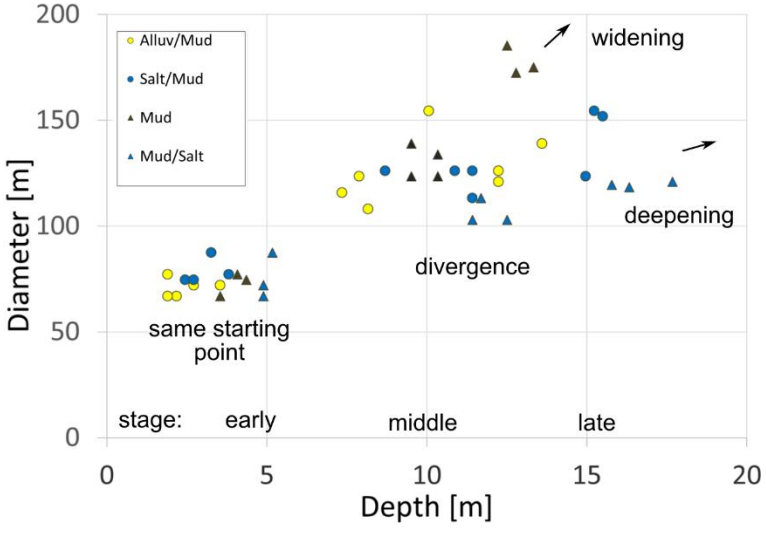

Figure 6: Depth versus diameter for different stages of the final model large-scale depressions for different material combinations. A clear divergence can be observed between mud-rich subsurface and salt-rich subsurface models at the late stage of the simulation.

The influence of different positions and different speeds of distributed material removal zones have also been tested thoroughly and are shown in detail in Appendix A. In all material cases for scenario (1), i.e. constant subrosion level and rate, and regardless of the depth of the array, only large, array-scale depressions occur and no sinkholes form in relation to the individual

Solid Earth Discuss., https://doi.org/10.5194/se-2019-20
Manuscript under review for journal Solid Earth
Discussion started: 29 January 2019

cavities. A shallower cavity array leads only to segmentation of the sinking block and/or fracturing of the margins. Varying the speed of array-wide subrosion produces no discernible difference in model outcome.

Clearly, a differential cavity growth is essential for development of sinkholes within a larger-scale depression. This is even more pronounced with accelerating growth of the central voids. Additionally, and importantly, for reproducing the morphological features and the order of appearance of sinkholes relative to the larger-scale depression, as observed in the Dead Sea examples, a simulated deepening of the karstification/subrosion level, i.e. cavity growth scenario (2), is necessary.

3.2 Stresses in a multiple void space system

From comparison of numerical simulations of all tested scenarios and setups in the previous section and Appendix A, we conclude that the inter-cavity distance has an influence on the inter-sinkhole distance at surface and, more importantly, if the cavity distance is wide enough, i.e. larger than 25 m, no large-scale depressions would form but only sinkholes. These aspect are better understood when looking at the stress distribution patterns. The maximum shear stress around the cavity arrays in model cavity growth scenarios (1) and (2) is shown in Figure 7. We here compare two different material setups, strong alluvium on weak mud (Figure 7A) and weak mud on strong salt and alluvium (Figure 7B). A model of five void spaces at ~ 40 m depth at stages shortly after installing the void spaces, immediately before the collapse of the surrounding material or exactly during the collapse, is used for the same particle assembly. The differential subrosion scheme uses the same setup as in the model Figure 13G (Appendix A), without a deepening of the zone, to avoid effects of remnant stress distributions.

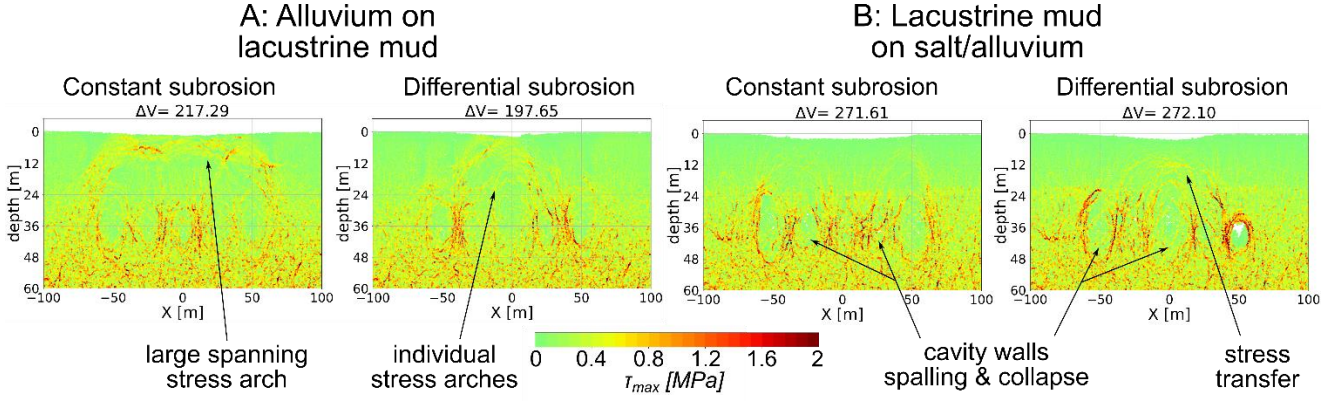

Figure 7: Maximum shear stress around void spaces for constant and differential subrosion models. Chosen are two material combinations where the subrosion affected layer differs in strength: (A) alluvium on mud multilayer and (B) mud on salt/alluvium succession. Shown are critical stages after void space installation followed by or exactly during overburden collapse for the same particle assembly. The removed volume [m^3] is shown above the plots.

Regarding the mechanical development, constant subrosion scenario (1) produce a shear stress arch spanning the whole system of void spaces, best visible in the alluvium on mud combination of Figure 7A. For differential subrosion scenario (2) without deepening, a complex pattern of individual, smaller stress concentrations appear with the maximum above the central, largest void. For the mud on salt/alluvium combination in Figure 7B, the weak overburden cannot sustain large stresses and both

Solid Earth Discuss., https://doi.org/10.5194/se-2019-20
Manuscript under review for journal Solid Earth
Discussion started: 29 January 2019

subrosion schemes produce individual stress arches around the cavities. The setup of a constant subrosion rate hence leads to a block-wise subsidence, while for differential subrosion, the interaction of stresses lead to multiple sinkhole development in a large-scale depression. Compare Appendix A.3 for compressive stresses.

3.3 Generic geophysical parameters

Figure 8 shows the results for the geophysical parameters to characterize the underground. As we consider a non-elastically deformed underground at a stage slightly before the next collapse, all derived parameters must be regarded as apparent. However, the usually short timescale on which seismic waves pass, makes the approach suitable for comparison with field data. We concentrate on a snapshot of the final deepening differential subrosion scenario (2) of alluvium on mud shortly before stage VI (cf. Figure 5A for the most important structural features). A deep and large depression zone with sinkholes has formed already. At this stage, the subrosion zone lies at ~ 50 m depth.

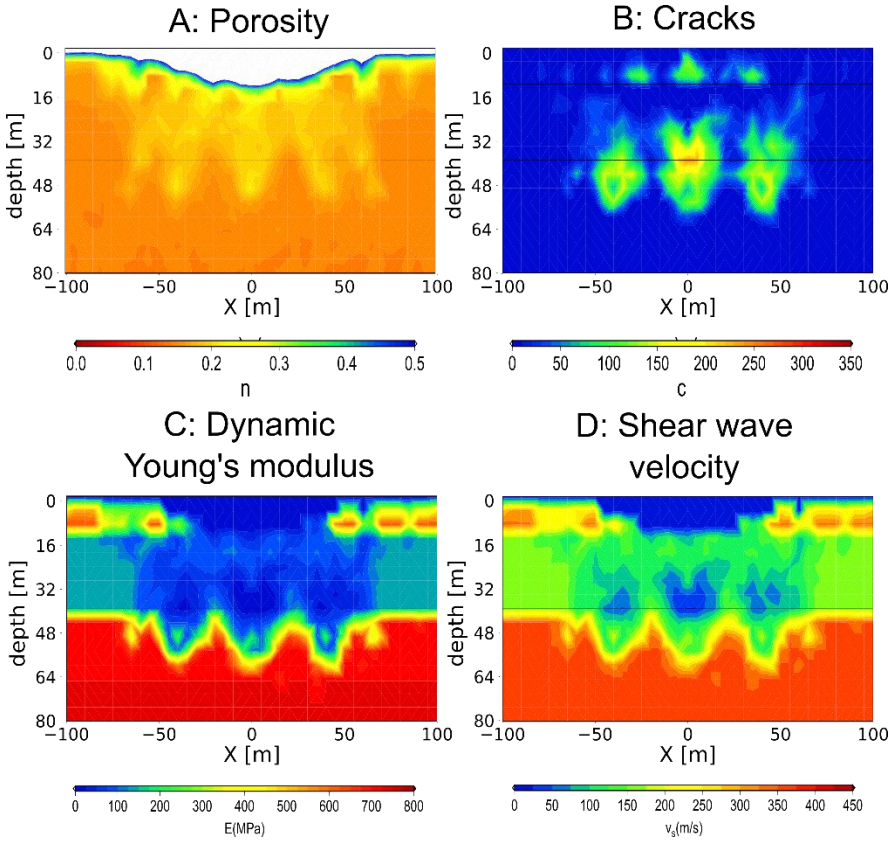

Figure 8: Geophysical characterization of the underground. Derived generic parameters for final model alluvium on mud shortly before stage VI (Figure 5A). (A) Porosity distribution. . (B) Number of cracks in the vicinity of the subrosion zone for this stage. (C) Apparent dynamic elastic (Young's) modulus (D) Apparent shear wave velocities. Black lines mark the limits of the mud horizon. The surface has collapsed partly into a depression plus sinkholes.

The porosity distribution at this stage can be seen in Figure 8A. It must be noted that porosities over 0.5 have not been translated into apparent elastic moduli, the latter is assumed to be zero then. The development leads to further cracking and subsidence of the overburden. The number of cracks is depicted in Figure 8B. Note that cracks in alluvium are counted in a cumulative way and cracks in mud are calculated per stage, due to the implemented healing procedure for broken bonds in mud (cf. Sec. 2 and Al-Halbouni et al., 2018). These cracks cause, in addition to the porosity, further changes of the apparent shear modulus and Poisson ratio and hence reduce the effective apparent elastic modulus of the underground (Figure 8C). This is also expressed in the apparent shear wave velocity of Figure 8D for the same stage. Hence these results show only a snapshot of a dynamic system. We observe strong changes in the central deep part of the model, where the largest void space growth rate exists. Remnants of earlier subrosion in shallower depth are nicely reflected in the apparent modulus and shear wave velocity distribution. More stable parts of the subsidence zone have higher values of $E > 500$ MPa and $v_S > 275$ m/s. The lowest values of $E < 100$ MPa and $v_S < 100$ m/s are close to the zones with highest porosity and most cracks. In between lies the low-velocity subrosion affected part both in the mud and alluvium layers.

4 Discussion

In this section, we discuss how realistic our numerical modelling results and simulated features are in comparison to natural observations and what can be deduced in terms of process understanding. We concentrate our comparison on results from remote sensing and geophysics for a very active sinkhole formation area at Ghor Al-Haditha at the Dead Sea. As a reminder, our model should be able to explain the following features typical for karst landform evolution:

- In all materials multiple sinkhole formations (aligned and/or nested).
- Larger-scale depression zones with pronounced deep cracks around.
- Formation before or at the same time when the first marginal cracks of the depression zones appear.
- Morphological differences depending in which material sinkholes/depressions form: Low depth/diameter (De/Di) ratio for mud-flat sinkholes, high De/Di for alluvium and thick salt ground cover and an order of magnitude lower ratios for large-scale depressions (Watson et al., 2019).
- Partly overhanging sides for sinkholes and depressions in high strength materials
- Lateral expansion of the depression in tandem with sinkhole migration.

4.1 Implications to karst landforms of clustered sinkholes and large-scale depressions

In our model results we observe main morphometric attributes of uvalas as composed by Gutiérrez and Lizaga, 2016 – a sharp increase in the area and long axis of the depression and a decrease in sinkhole density if measured by depressions per unit area. However, as discussed by Ćalić (2011) for limestone karst areas, differences between the depression types occur in regard to scale, inter-relationship and morphometry. Doline diameters occur on a sub-100m scale, uvalas typically occur on a several

Solid Earth Discuss., https://doi.org/10.5194/se-2019-20
Manuscript under review for journal Solid Earth
Discussion started: 29 January 2019

hundred meter to km-scale in limestone karst, and so called poljes on even a larger scale. A single uvala typically includes numerous dolines within it, which led to the concept of uvala formation by doline coalescence (Gutiérrez et al., 2014; Waltham et al., 2005). The cyclic concept of karst evolution, whereby dolines evolve to uvalas and ultimately to poljes, has been particularly heavily criticised and is regarded by most workers as erroneous. Nevertheless, regarding these postulated mechanisms for large-scale depression formation, and at least with respect to the examples in our study area, we can (1) preclude the mechanism of surface dissolution, as the many surfaces affected are non-karstic (non-soluble alluvium) and (2) we cannot preclude sinkhole coalescence as a mechanism for uvala formation, as such is observed in the strong interlayer models. However, these simulations are purely mechanical and hence the important hydrological aspects for the correct definition of the terms for areas of limestone or gypsum karst are beyond the scope of the current study to resolve.

Our models generally show that for multiple and nested sinkhole formation in large scale depressions and their correct order of appearance, a differential subrosion pattern with continuous deepening of the level needs to be implemented in the mechanical models. A spatially constant growth rate across the cavity array alone is not sufficient to generate sinkhole clusters, even if the interacting cavities were at different depths. This is due to the developed stress system. A concentrated stress arch would span a constant growth void space system while a differential growth produces a fragmented, interacting stress system.

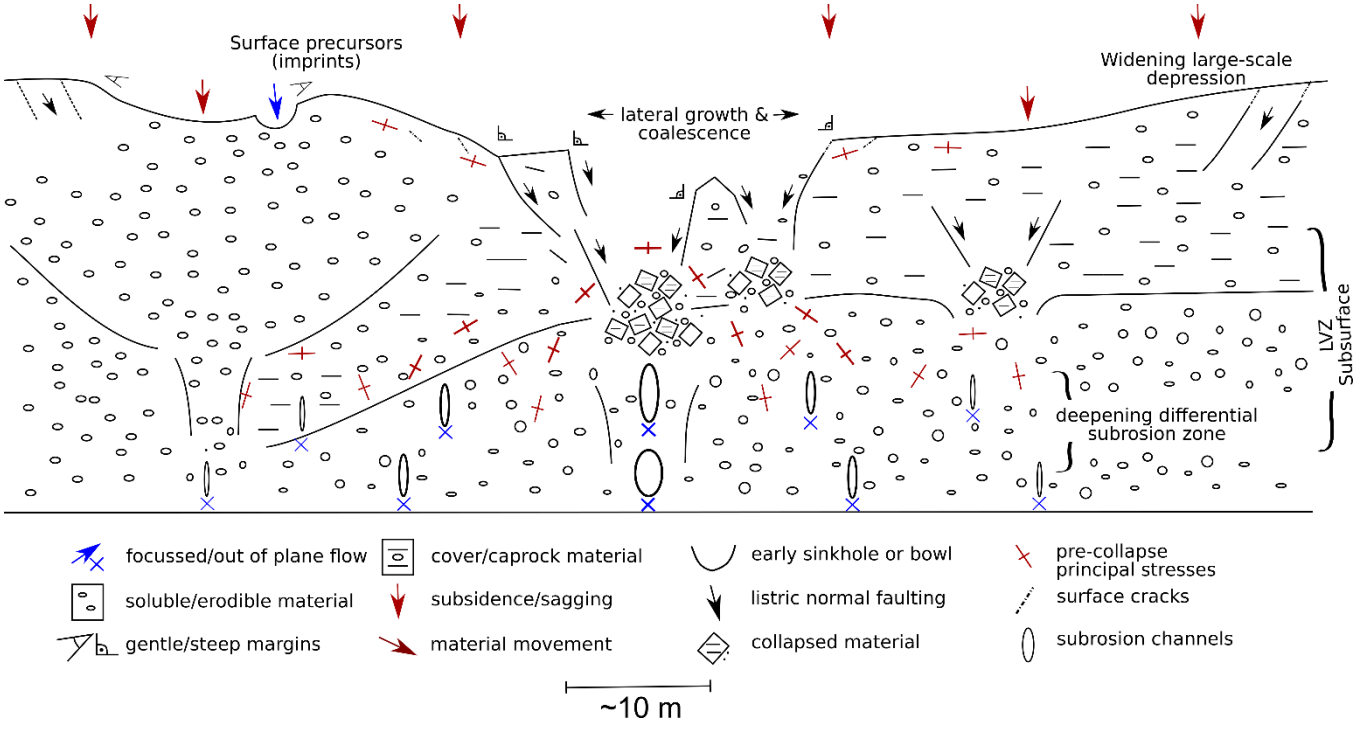

Figure 9: Conceptual model of sinkhole cluster and large-scale depression development. Several sinkholes of different stages, types and varying subrosion depths are indicated in this sketch (centre - caprock sinkholes, left - suffosion sinkhole).

Such a complex, dynamic karst system is depicted in a conceptual model in Figure 9 and summarizes the main findings of this study. A large-scale depression builds up due to distributed material removal in the underground by subrosion in a karstic drainage network. Nests of sinkholes may appear with relatively stable blocks in between. Lateral material heterogeneities, i.e. here a system of dipping layers, may cause different sinkhole morphologies and surface expressions of cracks that surround the large-scale depression. Depending on the material strength, large-scale depressions may build up either by sagging, block-wise brittle failure, lateral widening or coalescence of sinkholes. Water infiltration may cause additional superficial dissolution structures. The subsurface generally shows strong layering disturbances and porosity and modulus changes leading to a low seismic velocity zone (LVZ). The pre-collapse principal stress system is divided into individual stress arches due to the differential subrosion pattern.

The material removal procedure of the modelling approach can be regarded as the mechanical proxies to simulate a branched network of a karst flow system with preferential flow paths and a subsequent deepening by base-level fall. Our results provide an important verification of how these processes mechanically affect subsidence formation in karst regions with similar hydrogeological background. The widening of the flow system is hereby a typical observed hydrogeological condition of the current Dead Sea system due to the rapid base-level fall. In the following paragraph, we compare our model outcomes to morphological and geophysical results from the field site of Ghor Al-Haditha.

4.2 Comparison with observations from the Dead Sea sinkhole area

We analysed data from repeated photogrammetry of three consecutive years of the sinkhole area of Ghor Al-Haditha, at the eastern side of the Dead Sea (Figure 1A and Al-Halbouni et al., 2017). The datasets have been used to derive DSM difference maps between the consecutive years via GIS software.

Figure 10 shows the spatio-temporal evolution of recent sinkhole formations and patterns of holes, drainage channels, cracks and depression structures as observed in all cover materials in and around the main depression zone of the area (cf. Figure 1 and Figure 2). In the relatively strong alluvial sandy-gravel cover material (Figure 10A), we observe a cluster of rather deep and narrow sinkhole forming between 2014 and 2015. Small conical holes similar are precursors to the development of larger 1conical sinkholes (I and II). A typical coalescence and partial overprinting of large and small holes can be seen at the lower right (III). The DSM difference in Figure 10A depicts the new sinkholes and lateral sinkhole growth. We observe ae small overall subsidence between the new sinkholes, but a rather stable immediate surrounding.

In the relatively weak clayey limestone carbonates material (Figure 10B), we observe the development of a cluster of typical, wide and shallow sinkholes formed between 2015 and 2016. Similar to the alluvium, coalescence of individual holes into larger ones as well as the alignment of a series of different sized holes are observed and indicate a temporal evolution. The development of new collapses during one year in this material can either show possible precursory structures, e.g. re-activated sinkholes (IV), or not (V). The scarps are generally not stable in time (VI) due to numerous nests and generations of holes, as seen in the DSM difference map. An overall general subsidence of approximately 0.5 m +- 0.2 m is observed in the mud.

Solid Earth Discuss., https://doi.org/10.5194/se-2019-20
Manuscript under review for journal Solid Earth
Discussion started: 29 January 2019

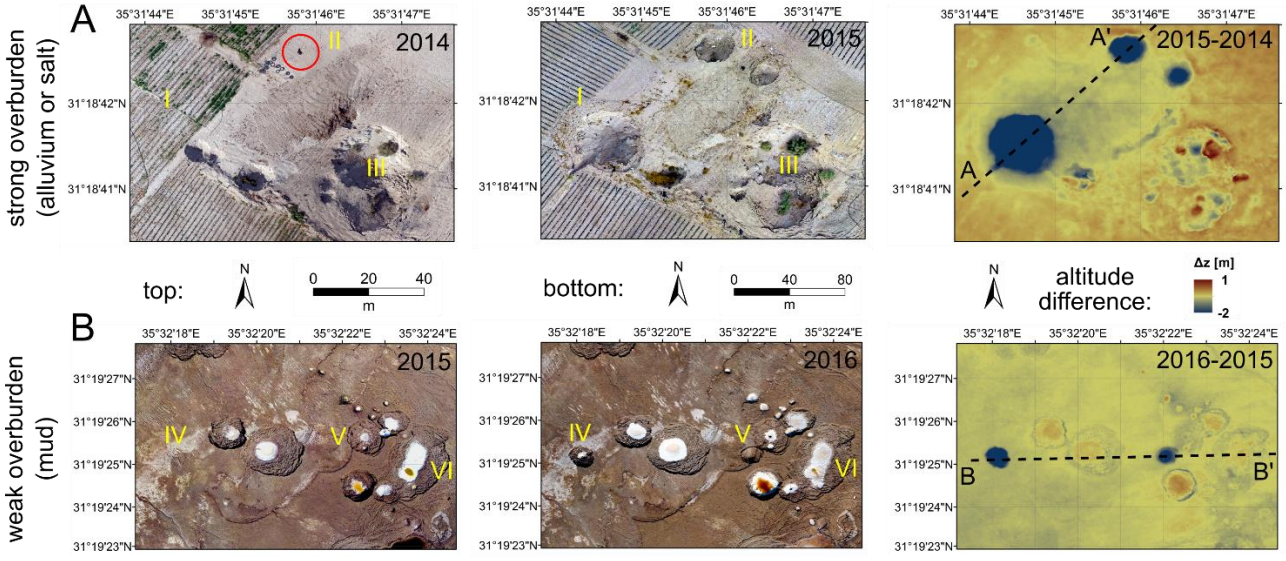

Figure 10: Examples for subsidence and sinkhole formation at Ghor Al-Haditha from orthophotos and DSM difference maps. All orthophotos and DSMs have the same resolution (10 cm px^{-1}) and the accuracies are (horizontal, vertical): 2014 (10 cm, 11 cm), 2015 (12, 17 cm) and 2016 (37, 31 cm). (A) Vertical displacement between 2014 and 2015 in the alluvium. Large sinkholes have formed in the alluvium (I, II) with slight overall subsidence along cross-section A-A' from SW-NE. Red circle marks a small precursory hole at (II). Vegetation growth may cover subsidence effects in coalesced sinkholes (III). (B) Vertical displacement changes between 2015 and 2016 in the mud-flat. Precursory information (re-activated sinkholes) may exist (IV) or not be visible (V). Nests of sinkholes exist (VI) in an area of pronounced overall subsidence of 0.5 m +- 0.2 m determined for cross-section B-B' from W-E. Compare topographic profiles in Figure 11.

For qualitative comparison with our models, Figure 11 shows the profiles across the DSM and vertical surface displacement for different stages of our models for weak and strong overburden. Although a precise matching is not intended, we clearly observe similar features there for the sinkholes/depression system at the Dead Sea. In weak material, slight subsidence at the early stage is visible, so-called imprints, which were also observed in the field. In strong material conical, early collapse sinkholes may precursor further large-scale collapses and nesting. The holes are usually accompanied by deep fractures in strong material and small, shallow fractures in the cohesive weak material, which indicate a widening of the depression zone.

Solid Earth Discuss., https://doi.org/10.5194/se-2019-20
Manuscript under review for journal Solid Earth
Discussion started: 29 January 2019

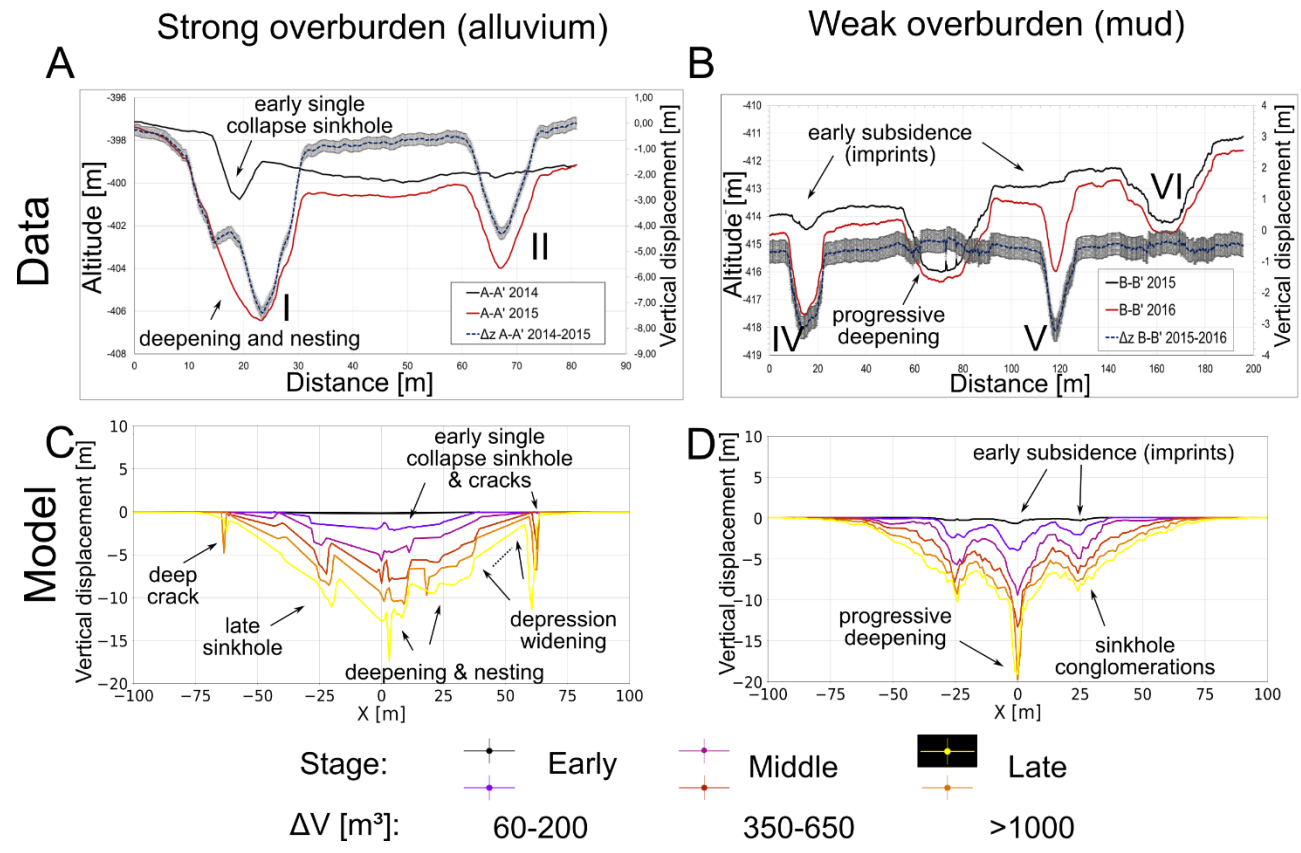

Figure 11: Topographic profiles data and models. Top row: Topography and vertical displacementFigure 10 of (A) cross-section A-A' from SW-NE in the alluvium and (B) cross-section B-B' from W-E in the mud-flat. Bottom row: Representative topographic profiles across final models for (C) high strength alluvium on mud and (D) low-strength lacustrine mud.

De/Di ratios for modelled sinkholes (Sec. 3.1) are generally consistent with field measurements (Al-Halbouni et al., 2017) and results from single void growth DEM models in Al-Halbouni et al., (2018) where the detailed evolution of sinkholes at Ghor Al-Haditha has been discussed. The results for large-scale depressions are an order of magnitude lower for the early stage depression development, as expected from remote sensing based estimations (Watson et al., 2019).

Finally, analysis of our model assemblies shows that holes at the surface, except the central one, usually grow quite randomly distributed. Clusters develop depending on the mechanical strength distribution and initiation of bond failure. Furthermore, because of the prescribed geometry of the subrosion zone, which is expected to be more complex in natural karst systems, and the limitation to 2D modelling, we cannot infer conclusions about the migration of such sinkhole clusters.

4.3 Subsurface patterns of sinkhole cluster and subrosion

From shear wave reflection seismics, zones with low reflectivity and velocity inversion anomalies in the S-wave velocity field are indicators for zones of material depletion or faults (Wadas et al., 2016). In the central part of the sinkhole affected alluvial

Solid Earth Discuss., https://doi.org/10.5194/se-2019-20
Manuscript under review for journal Solid Earth
Discussion started: 29 January 2019

fan system at Ghor Al-Haditha, a deep-seated (> 60 m depth) main subrosion zone based on the determined top of a lacustrine mud layer has been identified by comparison of shear wave reflection with borehole results (Polom et al., 2018). In several profiles of that work also shallower subrosion zones can be identified in the profiles and a general dip tendency of the deeper layers towards the NW is observed, indicating a Gilbert type alluvial fan foreset/topset system. We picked exemplarily profile one of Polom et al., (2018) and present an interpreted version of the shallower part in Figure 12A. A layered system of alluvial fan sediments with stronger reflections can be seen to the SW, while the central and NE part, close to the main depression zone, is affected by downsagging of up to several meters, disturbed layers, bowl- or cone shaped features in the upper 50 m and shifted layers indicating local fracturing. This is comparable to the subsurface structure as found in the final stages of the alluvium on mud model (Figure 5A). An indication of a deepening subrosion zone can be inferred from the large-scale bend continuation of the layers.

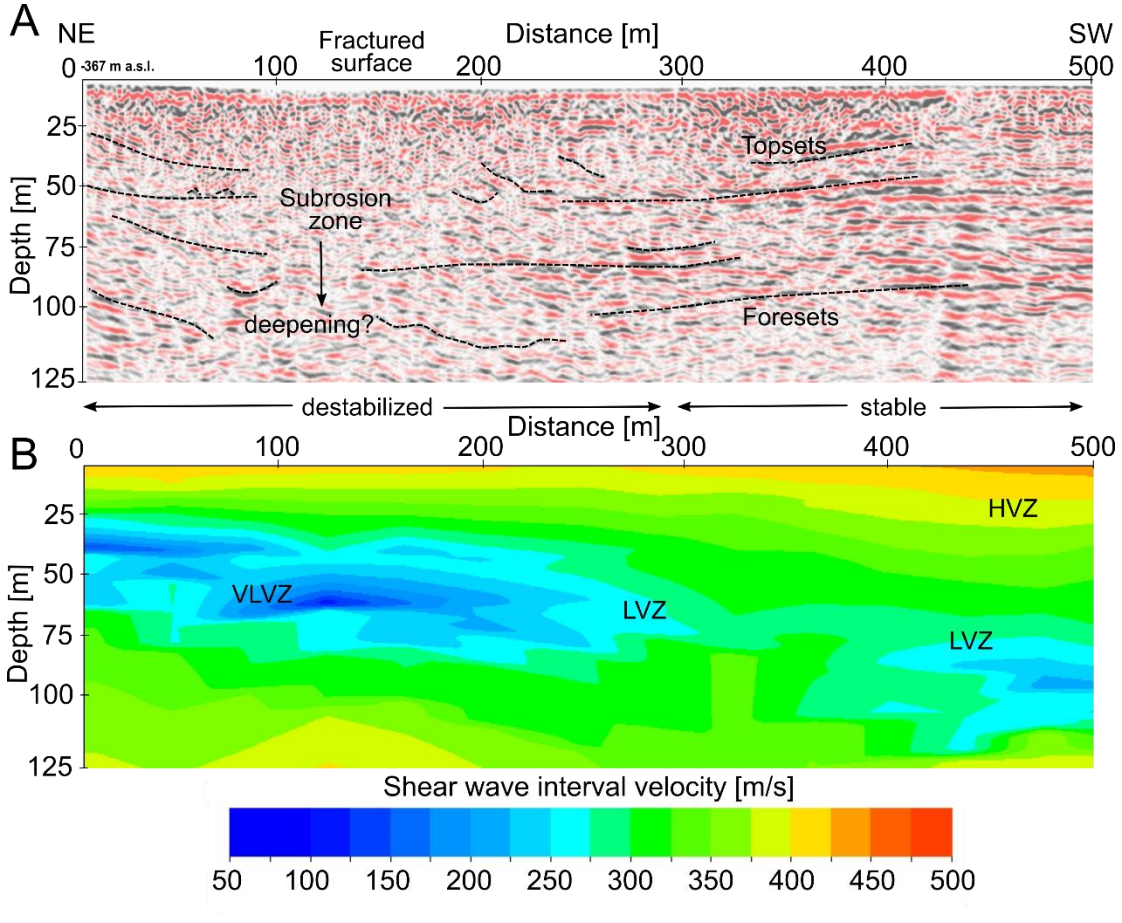

Figure 12: Subrosion affected parts of shear wave reflection seismic profile 1 at the sinkhole site of Ghor Al-Haditha. (A) Modified and interpreted first 500 m of profile 1 after *Polom et al.*, 2018**. (B) Shear wave interval velocity versus depth with marked very low (VLVZ), low (LVZ) and high velocity zones (HVZ).**

Solid Earth Discuss., https://doi.org/10.5194/se-2019-20
Manuscript under review for journal Solid Earth
Discussion started: 29 January 2019

Figure 12B shows the 2D-field of shear wave interval velocities in depth of the same profile section. It was derived after Dix, (1955) based on the 2D Root Mean Square (RMS) mean velocity field in time resulting iteratively from interactive velocity analysis of the hyperbola moveouts for the Common Midpoint (CMP) stacking procedure, which was subsequently iteratively evaluated and optimized by migration velocity analysis. The velocity field reflects the general survey situation of a relatively high velocity of 400-425 m/s close to the surface caused by the road construction (asphalt surface over a compacted man-made gravel infill) and reduced velocities of 300-375 m/s below for the natural alluvial sediments. The lateral structure mainly correlates with the structure image in Figure 12A. Low velocity values of 275 m/s down to ca.100 m/s (light blue to blue zones) indicate either subsurface zones of true low velocities due the specific lithologic formation, i.e. soft sediments, or zones of disturbed formations where the shear modulus is reduced due to mechanical stress of the formation by disruptions caused by up growing sinkhole processes. Very low values below 100 m/s may indicate areas where the shear wave could not propagate the area by a straight ray path and turned around it, e.g. in case of a cavity ($G_{dyn} = 0$) or a collapsed zone of very low shear modulus. In this case the resulting elongated propagating paths compared to the regular straight paths lead to zones of apparently very low interval velocities less than 100 m/s, partly close to zero, which are not realistic for true lithologic units. The decrease in apparent seismic shear wave velocity has been attributed by (Polom et al., 2018) to diminished grain coupling (either by pore pressure effects or enhanced fracturing of the rocks) and to the influence of a high-velocity surface layer (e.g. asphalt). The simulated apparent velocity values of Sec. 3.3 lie in the range of the field estimates with a strong reduction in the simulated mud layer during cracking and collapse. We consider the presented simulation stage of Figure 8 as most appropriate to explain the shear wave velocity reduction by enhanced fracturing, i.e. crack density increase, porosity increase and modulus reduction in a deepening differential subrosion zone. But, as these are generally transient parameters derived during or slightly before a collapse occurs, the determination in the field is dependent, additionally to possible resolution issues, on the time scale the collapse happens. Our final model successfully simulates both qualitatively and quantitatively subsurface patterns for the material combination as found at Ghor Al-Haditha field site.

5 Summary and conclusions

In this study, we presented a physically realistic 2D distinct element numerical modelling approach to simulate the growth of system (array) of karstic cavities with subsequent multiple sinkhole and large-scale depression formation. Two end-member growth scenarios of the multiple cavity array were tested with the following main outcomes:

1. Cavity growth at the same level and at the same individual growth rate yields a stable compression arch around the cavity array. This hinders individual sinkhole collapses but favours a large-scale (array-wide) block-wise subsidence.
2. Cavity growth at progressively deepening levels with varying individual growth rates is characterised by a heterogeneous, interacting stress pattern in the cavity array and overburden. This favours the formation of individual sinkholes, sinkhole clusters and uvala-like large-scale depressions.

The influences of the individual processes in growth scenario (2) are further investigated by comparison with surface morphologies from remote sensing and subsurface structures from geophysical studies at the active sinkhole formation area near Ghor Al-Haditha, at the Dead Sea. For this, we simulated four different layered combinations of low- and high strength materials. We found that:

- A variable void formation speed is necessary to form sinkhole cluster structures. This system can be compared to a distributed but focussed subrosion in preferential flow paths typical for karst systems.
- Deepening of the subrosion zone leads to a correct order of appearance of sinkholes relative to the larger-scale depression. This system is characteristic for a base-level fall as observed at the Dead Sea shoreline.
- Sinkholes for models with weak cavity-hosting material form synchronously with, or just before, the development of a larger-scale synclinal depression. For models with a strong cavity-hosting material large cavities can develop before the overburden collapses into them and large-scale depressions form mainly by nesting and coalescence of the holes.
- Observed morphometric relations (depths and diameters) for both sinkholes and large-scale depressions are successfully reproduced.
- Developed subsurface structures and calculated shear wave velocities match to a high degree to field estimations. A low seismic velocity zone (100-275 m/s) is imaged and simulated, compatible with the existence of a deepening subrosion zone at the field site.

Finally, we can conclude that the presented multiple void space growth numerical modelling approach has proven to be successfully applicable to sinkhole-depression systems and is of high general importance for mechanical understanding of karst development and hazard assessment.

Acknowledgements

We would like to acknowledge our colleagues from MEMR, namely Ali Sawarieh and Hussam Alrshdan, for their continuous support. Particular thanks go to Damien Closson, Thomas R. Walter, Marc K. Elmouttie and Charlotte M. Krawczyk. We would additionally like to thank the anonymous reviewers and the editor for the fruitful discussion. The authors acknowledge the financial support by the Helmholtz DESERVE Virtual Institute and the Federal Ministry of Education and Research of Germany in the framework of SIMULTAN (grant 03G0843). Finally, particular thanks go to Itasca for providing the license of PFC-V5 in the framework of the IEP and the German Academic Exchange Service (DAAD) for a short-term Doctorate research grant.

References

Al-Halbouni, D., Holohan, E. P., Saberi, L., Alrshdan, H., Sawarieh, A., Closson, D., Walter, T. R. and Dahm, T.: Sinkholes, subsidence and subrosion on the eastern shore of the Dead Sea as revealed by a close-range photogrammetric survey, Geomorphology, 285, 305–324, doi:10.1016/j.geomorph.2017.02.006, 2017.

Al-Halbouni, D., Holohan, E. P., Taheri, A., Schöpfer, M. P. J., Emam, S. and Dahm, T.: Geomechanical modelling of sinkhole development using Distinct Elements : Model verification for a single void space and application to the Dead Sea area, Solid Earth, 9 (Environmental changes and hazards in the Dead Sea region), 1341–1373, doi:https://doi.org/10.5194/se-2018-62, 2018.

Atzori, S., Antonioli, A., Salvi, S. and Baer, G.: InSAR-based modeling and analysis of sinkholes along the Dead Sea coastline, Geophys. Res. Lett., 42, 8383–8390, doi:10.1002/2015GL066053, 2015.

Baryakh, A. A., Rusin, E. P., Stazhevsky, S. B., Fedoseev, A. K. and Khan, G. N.: Stress-strain state of Karst areas, J. Min. Sci., 45(6), 3–10, 2009.

BGR, IAH, KIT and UNESCO: World Karst Aquifer Map, 1 : 40 000 000, Berlin, Reading, Karlsruhe, Paris., 2017.

Ćalić, J.: Karstic uvala revisited: Toward a redefinition of the term, Geomorphology, 134(1–2), 32–42, doi:10.1016/j.geomorph.2011.06.029, 2011.

Chen, Z., Auler, A. S., Bakalowicz, M., Drew, D., Griger, F., Hartmann, J., Jiang, G., Moosdorf, N., Richts, A., Stevanovic, Z., Veni, G. and Goldscheider, N.: The World Karst Aquifer Mapping project: concept, mapping procedure and map of Europe, Hydrogeol. J., 25(3), 771–785, doi:10.1007/s10040-016-1519-3, 2017.

Cundall, P. A.: A computer model for simulating progressive large scale movements in blocky rock systems, Proc. Symp. Rock Fract. (ISRM), Nancy, 1 [online] Available from: citeulike-article-id:11887443, 1971.

Cundall, P. A. and Strack, O. D. L.: A discrete numerical model for granular assemblies, Géotechnique, 29(1), 47–65, 1979.

Dahm, T. and Becker, T.: On the elastic and viscous properties of media containing strongly interacting in-plane cracks, Pure Appl. Geophys., 151(1), 1–16, doi:10.1007/s000240050102, 1998.

Dix, C. H.: Seismic velocities from surface measurements, Geophysics, XX(1), 68–86, 1955.

Dreybrodt, W., Gabrovšek, F. and Romanov, D.: Processes of a Speleogenessis: A Modeling Approach, Založba ZRC., 2005.

Fazio, N. L., Perrotti, M., Lollino, P., Parise, M., Vattano, M., Madonia, G. and Di Maggio, C.: A three-dimensional back-analysis of the collapse of an underground cavity in soft rocks, Eng. Geol., 228, 301–311, doi:10.1016/j.enggeo.2017.08.014, 2017.

Filin, S., Baruch, A., Avni, Y. and Marco, S.: Sinkhole characterization in the Dead Sea area using airborne laser scanning, Nat. Hazards, 58(3), 1135–1154, doi:10.1007/s11069-011-9718-7, 2011.

Gutiérrez, F. and Lizaga, I.: Sinkholes, collapse structures and large landslides in an active salt dome submerged by a reservoir: The unique case of the Ambal ridge in the Karun River, Zagros Mountains, Iran, Geomorphology, 254, 88–103, 2016.

Gutiérrez, F., Parise, M., De Waele, J. and Jourde, H.: A review on natural and human-induced geohazards and impacts in karst, Earth-Science Rev., 138, 61–88, doi:10.1016/j.earscirev.2014.08.002, 2014.

Hammam, A. H. and Eliwa, M.: Comparison between results of dynamic and static moduli of soil determined by different methods, HBRC J., 9(2), 144–149, doi:10.1016/j.hbrcj.2013.05.002, 2013.

Hatzor, Y. H., Wainshtein, I. and Bakun Mazor, D.: Stability of shallow karstic caverns in blocky rock masses, Int. J. Rock Mech. Min. Sci., 47(8), 1289–1303, doi:10.1016/j.ijrmms.2010.09.014, 2010.

Hazzard, J. F.: Acoustic Emission Calculation in PFC5.0, Minneapolis, Minnesota, USA., 2014.

Hazzard, J. F. and Young, R. P.: Dynamic modelling of induced seismicity, Int. J. Rock Mech. Min. Sci., 41(8), 1365–1376, doi:10.1016/j.ijrmms.2004.09.005, 2004.

Itasca Cooperation Group, I.: PFC 5.0 Manual, 2014.

Jing, L. and Stephansson, O.: Fundamentals of Discrete Element Methods for Rock Engineering, Elsevier., 2007.

Kaufmann, G. and Dreybrodt, W.: Calcite dissolution kinetics in the system CaCO3-H2O-CO2 at high undersaturation, Geochim. Cosmochim. Acta, 71(6), 1398–1410, doi:10.1016/j.gca.2006.10.024, 2007.

Parise, M. and Lollino, P.: A preliminary analysis of failure mechanisms in karst and man-made underground caves in Southern Italy, Geomorphology, 134(1–2), 132–143, doi:10.1016/j.geomorph.2011.06.008, 2011.

Polom, U., Alrshdan, H., Al-Halbouni, D., Dahm, T., Sawarieh, A., Atallah, M. Y. and Krawczyk, C. M.: Shear wave reflection seismics yields subsurface dissolution and subrosion patterns: application to the Ghor Al-Haditha sinkhole site, Dead Sea, Jordan, Solid Earth, 9 (Environmental Changes and Hazards in the Dead Sea Region), 1079–1098, doi:https://doi.org/10.5194/se-9-1079-2018, 2018.

Potyondy, D. O.: The bonded-particle model as a tool for rock mechanics research and application: current trends and future directions, Geosystem Eng., 17(6), 342–369, 2014.

Potyondy, D. O. and Cundall, P. A.: A bonded-particle model for rock, Int. J. Rock Mech. Min. Sci., 41(8), 1329–1364, doi:10.1016/j.ijrmms.2004.09.011, 2004.

Romanov, D., Kaufmann, G. and Hiller, T.: Karstification of aquifers interspersed with non-soluble rocks: From basic principles towards case studies, Eng. Geol., 116(3–4), 261–273, doi:10.1016/j.enggeo.2010.09.008, 2010.

Schöpfer, M. P. J., Childs, C. and Walsh, J. J.: Two-dimensional distinct element modeling of the structure and growth of normal faults in multilayer sequences: 1. Model calibration, boundary conditions, and selected results, J. Geophys. Res., 112(B10401), doi:10.1029/2006JB004902, 2007.

Soldal, M. and Mondol, N. H.: Dynamic to static relationships of shear modulus for sand and sandstones, in Thrid international Workshop on Rock Physics, Perth, Australia., 2015.

Tharp, T. M.: Mechanics of upward propagation of cover-collapse sinkholes, Eng. Geol., 52(1–2), 23–33, doi:10.1016/S0013-7952(98)00051-9, 1999.

Torremans, K.: Discrete element modeling experiments on the formation of layer-parallel veins in multilayer sequences, vol. 123, pp. 678–693., 2018.

Wadas, S. H., Polom, U. and Krawczyk, C.: High-resolution shear wave reflection seismics as a tool to image near-surface subrosion structures - a case study in Bad Frankenhausen, Germany, Solid Earth, 7, 1491–1508, doi:10.5194/se-7-1491-2016, 2016.

De Waele, J., Gutiérrez, F., Parise, M. and Plan, L.: Geomorphology and natural hazards in karst areas: A review, Geomorphology, 134(1–2), 1–8, doi:10.1016/j.geomorph.2011.08.001, 2011.

Waltham, T.: Control the drainage: the gospel accorded to sinkholes, Q. J. Eng. Geol. Hydrogeol., 49(1), 5–20, doi:10.1144/qjegh2015-088, 2016.

Waltham, T., Bell, F. and Culshaw, M. G.: Sinkholes and subsidence: Karst and Cavernous Rocks in Engineering and Construction, Springer, Berlin, Heidelberg., 2005.

Wang, C., Deng, A. and Taheri, A.: Three-dimensional discrete element modeling of direct shear test for granular rubber-sand, Comput. Geotech., 97, 204–216, doi:https://doi.org/10.1016/j.compgeo.2018.01.014, 2018.

Watson, R. A., Holohan, E. P., Al-Halbouni, D., Saberi, L., Sawarieh, A., Closson, D., Alrshdan, H., Abou Karaki, N., Walter, T. R. and Dahm, T.: Sinkholes, stream channels and base-level fall: a 50-year record of spatio-temporal development on the eastern shore of the Dead Sea, Solid Earth Discuss., doi:https://doi.org/10.5194/se-2018-105, 2019.

Weisbrod, N., Alon-Mordish, C., Konen, E. and Yechieli, Y.: Dynamic dissolution of halite rock during flow of diluted saline solutions, Geophys. Res. Lett., 39(9), 1–7, doi:10.1029/2012GL051306, 2012.

Wichtmann, T. and Triantafyllidis, T.: On the correlation of “static” and “dynamic” stiffness moduli of non-cohesive soils, Bautechnik, 86, 28–39, doi:10.1002/bate.200910039, 2009.

Yechieli, Y., Abelson, M. and Baer, G.: Sinkhole formation and subsidence along the Dead Sea coast, Israel, Hydrogeol. J., 24(3), 601–612, doi:10.1007/s10040-015-1338-y, 2016.

Solid Earth Discuss., https://doi.org/10.5194/se-2019-20
Manuscript under review for journal Solid Earth
Discussion started: 29 January 2019

Appendix A Numerical simulation of multiple void spaces with DEM

A.1 Cavity growth implementation

The cavity growth function f(i), which relates the initial removed area A_0 to the area increment to be removed A_i (Al-Halbouni et al., 2018), has been updated to account for multiple voids that can start and stop growing at defined intervals (i_0, i_{max}). The function hence depends on each single void of index j and the formula becomes:

$$A_i = f_j(i,..)A_0, \qquad i \in [i_0, i_{max}]$$

The linear void space growth function relating initial void space area with the removed area at further intervals stands as an approximation for real fracture or void growth by physio-chemical processes in karst aquifers. Pure chemical dissolution of limestone or gypsum hereby shows a linear behaviour as long as the concentration of the under saturated incoming fluid is lower than 90 % of the equilibrium concentration for that mineral (Dreybrodt et al., 2005; Kaufmann and Dreybrodt, 2007; Romanov et al., 2010).

A.2 Optimal model development

For finding the optimal model, we generally define five individual semi-elliptical voids with a distance of 25-40 m from each other. They belong to one of three initial size groups and one of three void space growth function classes. Initial areas of set 1 (small) are $A_{0,1} = 2.7 - 6$ m^3 and linear eccentricity $e_1 = 1.7 - 2.2$, of set 2 (mid-sized) $A_{0,2} = 10 - 14$ m^3 and $e_2 = 3.5 - 4.0$ and of set 3 (big) $A_{0,3} = 24.5$ m^3 and $e_3 = 5 - 5.5$ Material removal of set A (slow) has an incremental function of $f_{j=1}(i) = 1.0^i$, set B (mid-speed) $f_{j=2}(i) = 1.05 - 1.075^i$ and set C (fast) $f_{j=3}(i) = 1.1^i$. The subrosion zone is defined in different depth below the surface, set I (shallow) is for 20 m depth, set II (middle) for 30 m depth, set III (mid-deep) for 40 m depth, set IV (deep) stands for 50 m depth and set V (very deep) stands for 60 m depth. Representative for different material combinations all results of the tests are shown for alluvium on mud layer setup Figure 13. The following table summarizes the different tested void space setups. The results for the final (best) model are shown in Sec. 3.

Solid Earth Discuss., https://doi.org/10.5194/se-2019-20
Manuscript under review for journal Solid Earth
Discussion started: 29 January 2019

Table 3: Tested sets of void spaces for the DEM models. All of them were applied to the three material settings at the Dead Sea shoreline. The model set combination is given in terminology: Initial area set/void space growth class/subrosion depth set, so, e.g. 1/A/I would stand for small sized, shallow seated void spaces growing at a constant rate.

Removal zone/ model set name	A: All voids the same ($A_{0,2}$)	B: Three inner voids shallower ($A_{0,2}$)	C: Two outer voids shallower ($A_{0,2}$)	D: Two outer voids accelerating growth ($A_{0,2}$)	E: All voids differential growth rate but same initial areas ($A_{0,2}$)	F: All voids same growth rate but variable initial areas ($A_{0,2}, A_{0,3}$)	G: All voids differential growth rate and variable initial areas ($A_{0,1}, A_{0,2}, A_{0,3}$)	H: Deepening differential growth rate and variable initial areas ($A_{0,1}, A_{0,2}, A_{0,3}$)	I: Final model: Deepening differential growth rate and variable initial areas ($A_{0,1}, A_{0,2}, A_{0,3}$)
central	2/A/III	2/A/II	2/A/III	2/A/III	2/C/III	3/A/III	3/C/III	1: 3/C/I 2: 3/C/III 3: 3/C/V	1: 3/C/I 2: 3/C/II 3: 3/C/III 4: 3/C/IV
two inner	2/A/III	2/A/II	2/A/III	2/A/III	2/B/III	2/A/III	2/B/III	1: 2/B/I 2: 2/B/III 3: 2/B/V	1: 2/B/I 2: 2/B/II 3: 2/B/III 4: 2/B/IV
two outer	2/A/III	2/A/III	2/A/II	2/B/III	2/A/III	1/A/III	1/A/III	1: 1/A/I 2: 1/A/III 3: 1/A/V	1: 1/A/I 2: 1/A/II 3: 1/A/III 4: 1/A/IV

Constant void space growth: Figure 13A shows the evolution of a growing void space system of five voids of set A until surface collapse for multilayers of alluvium and mud. It shows cracks at the margins of the collapse zone and gradual sinking of a whole block. Individual, smaller scale sinkholes do not form.

Constant void space growth with shallower inner voids: Figure 13B shows the evolution of a growing void space system of five voids of set A with two inner voids 10 m higher than the others. It shows cracks at the margins of the collapse zone and gradual sinking of the whole block but with a division of the block into segments. Real individual smaller scale sinkholes do not form but are only an effect of the segmentation by the higher lying voids.

Solid Earth Discuss., https://doi.org/10.5194/se-2019-20
Manuscript under review for journal Solid Earth
Discussion started: 29 January 2019

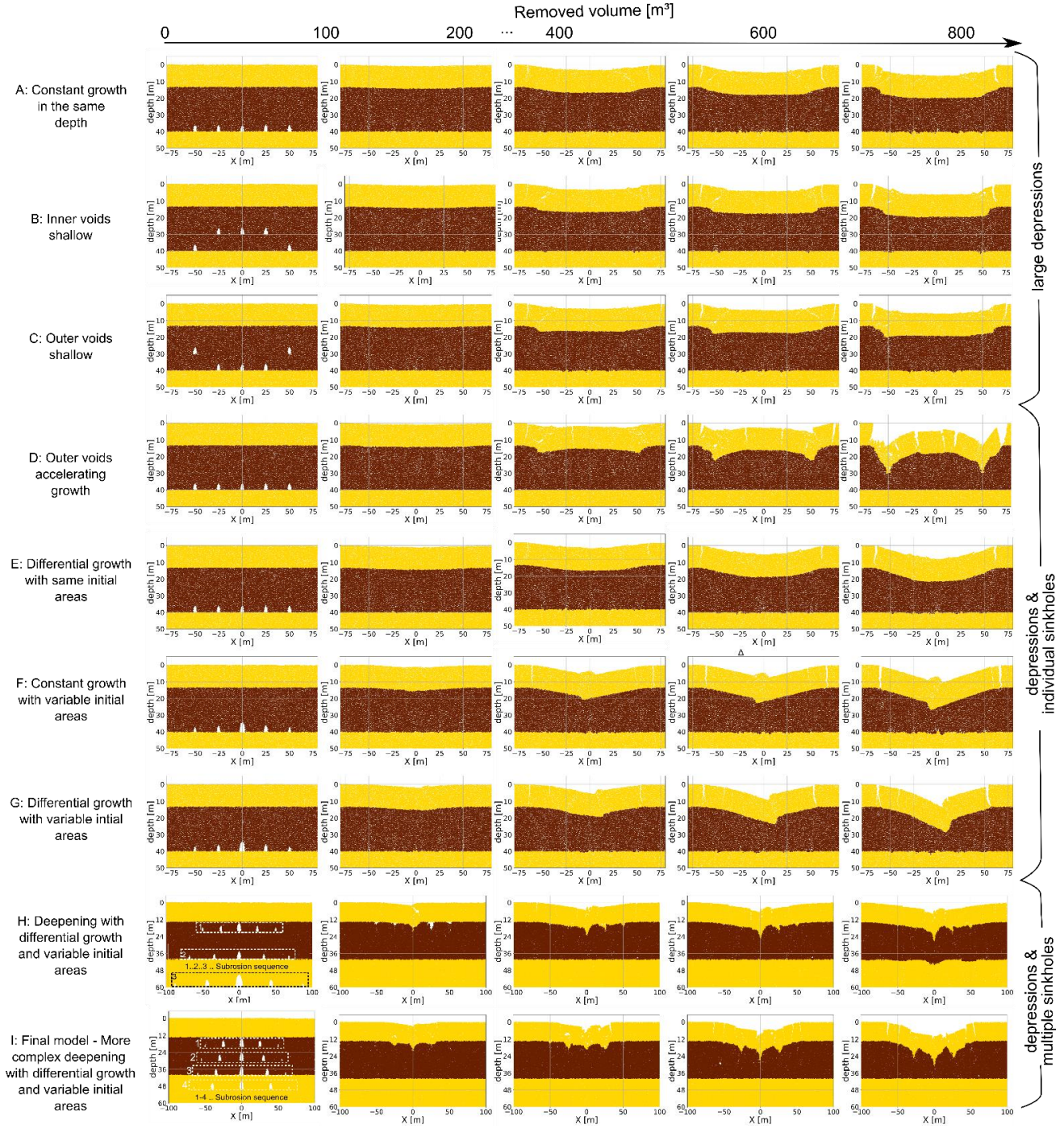

Figure 13: The influence of void space geometry (sizes and positions) and material removal speed in an alluvium on mud layered system. These simulations (A)-(I) are essential to determine step by step the optimal model setup to achieve multiple sinkhole collapses in a large depression zone. Shown are only the core zones of the models at different stages of removed volume indicated above each plot. Note the slightly different size of plots (H, I) in order to account for the widening and deepening subrosion zone.

Constant void space growth with shallower outer voids: Figure 13C shows the evolution of a growing void space system of five voids of set A with the two outer voids 10 m higher than the others. It shows cracks at the margins of the collapse zone and gradual sinking of the whole block and toppled blocks at the margins. Real individual, smaller scale sinkholes do not form, only a large and rather flat depression.

Accelerating growth of outer voids: Figure 13D shows the evolution of a growing void space system of three inner voids of set A with the two outer voids of set B, which leads effectively to an accelerated growth of the outer voids. We observe cracks and toppled blocks at the margins of the collapse zone, a gradual sinking of the whole block and first individual, but very large sinkholes. The deepest part of the depression is one of the sinkholes. The convex shaped bending of the middle part is not observed in our field study.

Differential growth with same initial areas: Figure 13E shows the evolution of a growing void space system of the 2 outer voids of set A, the two inner voids of set B and the central void of set C, effectively an accelerating growth for the inner voids. We find cracks and toppled blocks at the margins of the collapse zone, a gradual sinking of the whole block. A large-scale more steep sided depression forms.

Constant growth with variable initial areas: In Figure 13F the same effect as in the previous model can be produced by larger initial areas of the inner void spaces, with a largest material removal zone in the center. The growth rate is constant for each individual void space leading but the initial sizes differ. Here, we produce a compression ridge at the center of the depression zone.

Differential void space growth with variable initial areas: In Figure 13G a combination of a larger starting area with a fastest growing rate in the center as in Figure 13E and F is used to achieve an accelerating differential void space growth. We can see the same effect as in the previous models but with a first formation of a small scale sinkhole in the center of the depression.

Deepening differential void space growth: Figure 13H is a pre-final model accounting for the base-level fall affecting the subrosion zone depth. A combination of a larger starting area and deepening from levels I (20 m) to III (40 m) to V (60 m) is implemented, halting the previous subrosion when the new one is activated. We can see already complex structure of individual, nested sinkholes in a large scale depression. This process is refined for the final model shown in Figure 13I, using a more complex combination and intermediate steps of subrosion zone deepening from levels I to IV. This leads to clearer development of multiple nested sinkholes that subside into a large depression zone the deeper the subrosion zone lies.

Solid Earth Discuss., https://doi.org/10.5194/se-2019-20
Manuscript under review for journal Solid Earth
Discussion started: 29 January 2019

A.3 Principal stresses in a multiple void space system

Figure 14 and Figure 15 show the developed maximum and minimum compressive stress system for two model layer setups and the constant subrosion versus differential subrosion setups. A large compression arch spanning all void spaces develops for strong overburden material and constant subrosion scenario (1) but is more fragmented in the differential subrosion scenario (2, Figure 14A). For the weak overburden rather individual, stabilizing compressive arches build up in the strong interlayer and hardly translate upward (Figure 14B). The minimum compressive stress plots for both setups show similar behaviour. Tensile stresses are recorded near the surface for strong overburden material (Figure 15A). In contrast, the strong interlayer beneath the weak material leads to strong tensile stresses lined up at the edges of the cavities with spalling phenomena for both subrosion schemes. This line is centrally broken in the differential subrosion scheme (Figure 15B). Shear stress observations are discussed in Section 3.2.

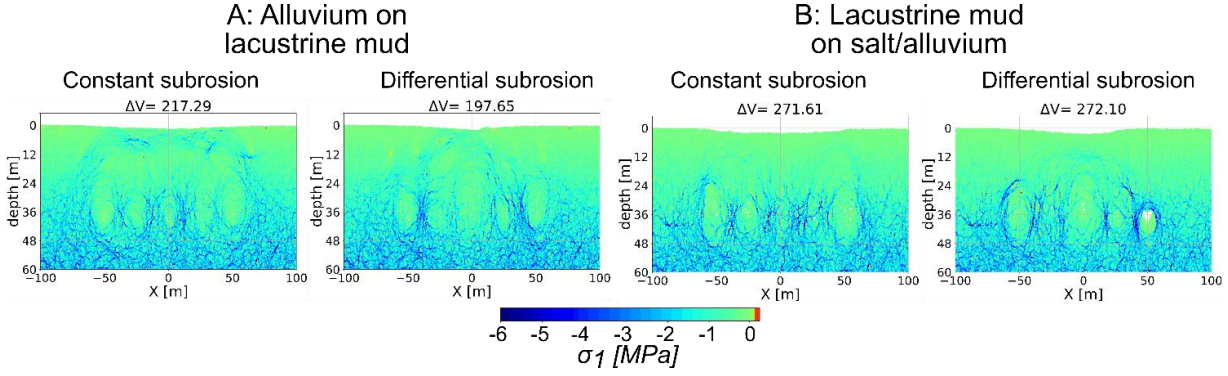

Figure 14: Maximum principal stress around void spaces for constant and differential subrosion models. Chosen are two material combinations where the subrosion affected layer differs in strength: (A) alluvium on mud multilayer and (B) mud on salt/alluvium succession Shown are critical stages after void space installation followed by or exactly during overburden collapse for the same particle assembly. The removed volume [m^3] is shown above the plots.

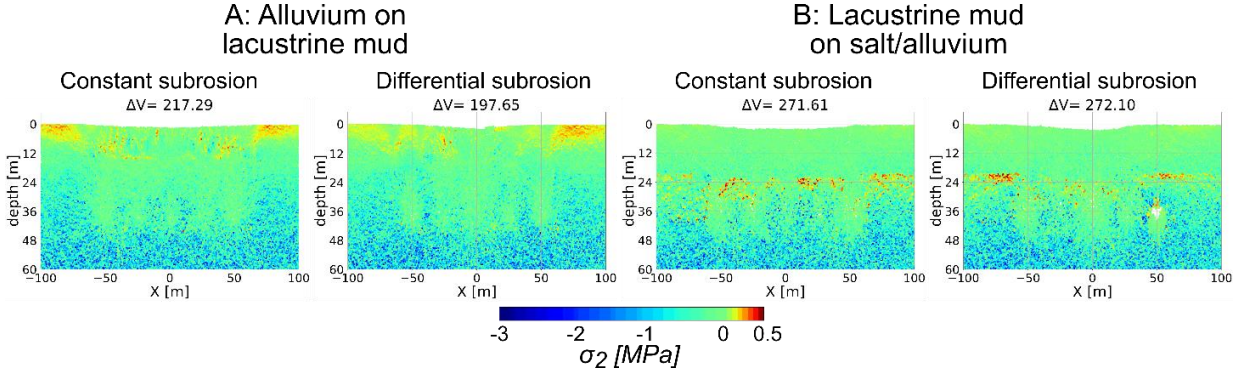

Figure 15: Minimum principal stress around void spaces for constant and differential subrosion models. Chosen are two material combinations where the subrosion affected layer differs in strength: (A) alluvium on mud multilayer and (B) mud on salt/alluvium succession. Shown are critical stages after void space installation followed by or exactly during overburden collapse for the same particle assembly. The removed volume [m^3] is shown above the plots.